



## BIOFABRICATION OF MULTISCALE BONE EXTRACELLULAR MATRIX SCAFFOLDS FOR BONE TISSUE ENGINEERING

F.E. Freeman<sup>1,2</sup>, D.C. Browe<sup>1,2</sup>, Diaz-Payno PJ<sup>1,2</sup>, J. Nulty<sup>1,2</sup>, S. Von Euw<sup>1,2</sup>, W.L. Grayson<sup>3,4,5,6</sup>  
and D.J. Kelly<sup>1,2,7,8,\*</sup>

<sup>1</sup>Trinity Centre for Biomedical Engineering, Trinity Biomedical Sciences Institute, Trinity College Dublin, Ireland

<sup>2</sup>Department of Mechanical and Manufacturing Engineering, School of Engineering, Trinity College Dublin, Ireland

<sup>3</sup>Department of Biomedical Engineering, Johns Hopkins University School of Medicine, Baltimore, MD, USA

<sup>4</sup>Translational Tissue Engineering Centre, Johns Hopkins University School of Medicine, Baltimore, MD, USA

<sup>5</sup>Department of Material Sciences and Engineering, Whiting School of Engineering, Johns Hopkins University, Baltimore, MD, USA

<sup>6</sup>Institute of Nanobiotechnology, Whiting School of Engineering, Johns Hopkins University, Baltimore, MD, USA

<sup>7</sup>Department of Anatomy, Royal College of Surgeons in Ireland, Dublin, Ireland.

<sup>8</sup>Advanced Materials and Bioengineering Research Centre (AMBER), Royal College of Surgeons in Ireland and Trinity College Dublin, Dublin, Ireland.

### Abstract

Interconnected porosity is critical to the design of regenerative scaffolds, as it permits cell migration, vascularisation and diffusion of nutrients and regulatory molecules inside the scaffold. 3D printing is a promising strategy to achieve this as it allows the control over scaffold pore size, porosity and interconnectivity. Thus, the aim of the present study was to integrate distinct biofabrication strategies to develop a multiscale porous scaffold that was not only mechanically functional at the time of implantation, but also facilitated rapid vascularisation and provided stem cells with appropriate cues to enable their differentiation into osteoblasts. To achieve this, polycaprolactone (PCL) was functionalised with decellularised bone extracellular matrix (ECM), to produce osteoinductive filaments for 3D printing. The addition of bone ECM to the PCL not only increased the mechanical properties of the resulting scaffold, but also increased cellular attachment and enhanced osteogenesis of mesenchymal stem cells (MSCs). *In vivo*, scaffold pore size determined the level of vascularisation, with a larger filament spacing supporting faster vessel in-growth and more new bone formation. By freeze-drying solubilised bone ECM within these 3D-printed scaffolds, it was possible to introduce a matrix network with microscale porosity that further enhanced cellular attachment *in vitro* and increased vessel infiltration and overall levels of new bone formation *in vivo*. To conclude, an “off-the-shelf” multiscale bone-ECM-derived scaffold was developed that was mechanically stable and, once implanted *in vivo*, will drive vascularisation and, ultimately, lead to bone regeneration.

**Keywords:** 3D printing, extracellular matrix, bone, tissue engineering, osteogenesis, mesenchymal stem cells.

**\*Address for correspondence:** Prof. Daniel Kelly, Trinity Centre for Biomedical Engineering, Trinity Biomedical Sciences Institute, Trinity College Dublin, Ireland.

Telephone number: +353 18963947 Email: KELLYD9@tcd.ie

**Copyright policy:** This article is distributed in accordance with Creative Commons Attribution Licence (<http://creativecommons.org/licenses/by-sa/4.0/>).

### Introduction

Tissue engineering is a multidisciplinary field that aims to enable repair or regeneration of damaged or diseased tissues using appropriate combinations

of cells, biomaterials and instructive signals (Reddi, 1998; Reddi, 2007). Despite decades of research, relatively few bone tissue engineering therapies have reached the clinic and those that have typically report poorer outcomes than in pre-clinical animal

trials (d'Aquino *et al.*, 2009; Hibi *et al.*, 2006; Krecic-Stres *et al.*, 2007; Lee *et al.*, 2010; Marcacci *et al.*, 2007; Meijer *et al.*, 2007; Meijer *et al.*, 2008; Quarto *et al.*, 2001; Shayesteh *et al.*, 2008; Zamiri *et al.*, 2013). Reasons for this are multi-faceted, including poor scaffold mechanical properties, poor implant vascularisation and inadequate new bone formation *in vivo* (Amini *et al.*, 2012; Ko *et al.*, 2007; O'Brien, 2011; Phelps and Garcia, 2009). Scaffold seeding with cells, in the attempt to first engineer a bone-like tissue *in vitro*, has proved challenging, with issues such as core degradation and poor implant integration limiting the success of such approaches (Amini *et al.*, 2012; Lyons *et al.*, 2010; O'Brien, 2011). Ideally, when designing scaffolds for bone tissue engineering, they should fulfil several key criteria. They should possess sufficient mechanical properties to support the defect region during regeneration. Their pore size and interconnectivity should allow cells, nutrients and other regulatory molecules to travel within the scaffold and facilitate vascularisation of the scaffold post-implantation (Habibovic *et al.*, 2008; Jones *et al.*, 2007; Müller *et al.*, 2009). The scaffold should also provide seeded cells or stem cells that migrate from the bone marrow and/or surrounding tissues into the scaffold post-implantation with appropriate biochemical and biophysical cues to enable their differentiation into osteoblasts.

Previously, porous bone scaffolds have been fabricated using a variety of techniques, including particle/salt leaching (Cao and Kuboyama, 2010), gas foaming (Kucharska *et al.*, 2012), freeze-drying (Sultana and Wang, 2008) and phase separation (Hutmacher, 2000). However, one of the major limitations to such techniques is the lack of control over pore size, porosity and interconnectivity of the pores and the overall scaffold geometry. This has led to increased interest in additive manufacturing and 3D printing for tissue engineering strategies. An obvious advantage of 3D printing for bone tissue engineering is the capacity to control scaffold pore size and interconnectivity, which in turn regulates angiogenesis and osteogenesis within the construct (Karageorgiou and Kaplan, 2005). The most commonly used synthetic polymers for 3D printing of bone tissue engineering scaffolds are polycaprolactone (PCL) (Daly *et al.*, 2016; De Santis *et al.*, 2011; Hung *et al.*, 2016; Kim and Son, 2009; Nyberg *et al.*, 2017; Park *et al.*, 2011; Park *et al.*, 2012; Seyednejad *et al.*, 2012; Temple *et al.*, 2014; Yilgor *et al.*, 2008) and poly(lactic-co-glycolic acid) (PLGA) (Ge *et al.*, 2009a; Ge *et al.*, 2009b; Guo *et al.*, 2017; Park *et al.*, 2012; Shim *et al.*, 2014). Although such synthetic polymers can be used to generate mechanically stable scaffolds, on their own, they are not osteoconductive. This can potentially be addressed by incorporating various forms of calcium phosphate within the synthetic polymers. The most commonly used calcium phosphate mineral additives are tricalcium phosphates (TCP) (Kang *et al.*, 2016; Ko *et al.*, 2007; Polini *et al.*, 2011; Rai *et al.*, 2010; Reichert *et al.*, 2011;

Yeo *et al.*, 2008; Yeo *et al.*, 2010) and hydroxyapatite crystals (HA) (Causa *et al.*, 2006; Guarino *et al.*, 2008; Heo *et al.*, 2009; Park *et al.*, 2011; Polini *et al.*, 2011). The addition of TCP or HA improves the mechanical properties of the resulting scaffold (Park *et al.*, 2011; Seyednejad *et al.*, 2012; Yeo *et al.*, 2008; Yeo *et al.*, 2010). Furthermore, *in vitro* studies have shown that the addition of calcium phosphate mineral additives to PCL can increase its osteo-inductivity (Causa *et al.*, 2006; Park *et al.*, 2011; Polini *et al.*, 2011; Rai *et al.*, 2010). *In vivo*, such composite scaffolds have also been shown to promote bone regeneration in different preclinical models (Heo *et al.*, 2009; Kim *et al.*, 2012; Reichert *et al.*, 2011). While such studies have generally reported benefits to the implantation of such constructs, in general, complete healing of the defects was not observed, pointing to the need for further improving the design of such implants.

One method for improving scaffold bioactivity is through the addition of extracellular matrix (ECM) components (Cheng *et al.*, 2014). Bone-ECM-based products are widely used clinically and can be divided into two classes, decellularised bone matrix (DCB) and demineralised bone matrix (DMB) (Cheng *et al.*, 2014). For example, Bio-Oss (Geistlich Biomaterials), a clinically available form of DCB, consists of mm-sized granules of bovine trabecular bone with most of the organic phase largely removed and has predominately been used in dental surgeries (Nyberg *et al.*, 2017). Previously, Nyberg *et al.* (2017) have compared the osteogenic potential *in vitro* of Bio-Oss versus a 30 % DCB/PCL blend and found there was no significant difference in osteogenic induction of adipose-derived mesenchymal stem cells (MSCs) cultured in hydrogels printed alongside the scaffolds (Nyberg *et al.*, 2017). The group went on to further demonstrate enhanced bone healing with the DCB blend in a mouse cranial defect model (Hung *et al.*, 2016). DMB is an allogenic bone graft material (Hung *et al.*, 2016; Nyberg *et al.*, 2017), which is obtained from xenogenic and allogenic sources and is commonly used in orthopaedic surgeries for filling in bony defects after fractures or tumour debulking (Cheng *et al.*, 2014; Drosos *et al.*, 2007). The general preparation of DMB usually involves the removal of soft tissue, blood and lipids, followed by antibiotic soaks, acid demineralisation and several rounds of freeze-drying (Gruskin *et al.*, 2012). The end-product is a composite of collagen types I, IV and X, as well as bone morphogenetic proteins (BMPs) and transforming growth factor-beta 1, 2 and 3, endowing it with osteoinductive properties (Cheng *et al.*, 2014; Gruskin *et al.*, 2012). However, a limitation of DMB are its poor mechanical properties, which is a problem when treating load-bearing bone defects. Furthermore, the processing of such bone-matrix-derived biomaterials into porous scaffolds with defined architectures optimised for angiogenesis and osteogenesis remains a challenge.

The aim of the study was to integrate multiple biofabrication strategies to develop multiscale porous

scaffolds for bone defect repair that were not only mechanically functional at the time of implantation, but which would also support vascular in-growth and provide skeletal stem cells with appropriate cues to enable their differentiation into osteoblasts. The macroscale architecture of the scaffolds was initially engineered using 3D printing of composite PCL and DCB filaments, where the porosity (filament spacing) was varied with the goal of maximising vascularisation and bone formation *in vivo*. In the second phase of the study, microscale porosity was introduced by freeze-drying solubilised bone ECM within the macroscale pores of the 3D-printed PCL-DCB to produce a multiscale scaffold. It was hypothesised that the incorporation of such microporous bone ECM into the body of 3D-printed scaffolds would enhance cellular attachment as well as vessel infiltration and bone formation *in vivo*.

## Materials and Methods

### Generation of DCB

DCB was generated from cow tibiae obtained from an abattoir, as previously described (Hung *et al.*, 2016; Nyberg *et al.*, 2017). Briefly, this was achieved by blasting bovine bone fragments with water to remove all of the bone marrow. Then, the bone fragments were placed in a series of four detergent washes: 0.1 % ethylenediaminetetraacetic acid (EDTA) for 1 h, 0.1 % EDTA/10 mM Tris for 12 h, 0.5 % sodium dodecyl sulphate (SDS)/10 mM Tris for 24 h and 50 U/mL DNase, 1 U/mL RNase, 0.1 % EDTA/10 mM Tris for 5 h (all from Sigma-Aldrich). Following the washes, the bone was rinsed with phosphate-buffered saline (PBS) and lyophilised. Decellularised bone fragments were cryomilled with a Spex 6870 Freezer Mill (SPEX, Stanmore, UK) to form a powder. Quant-

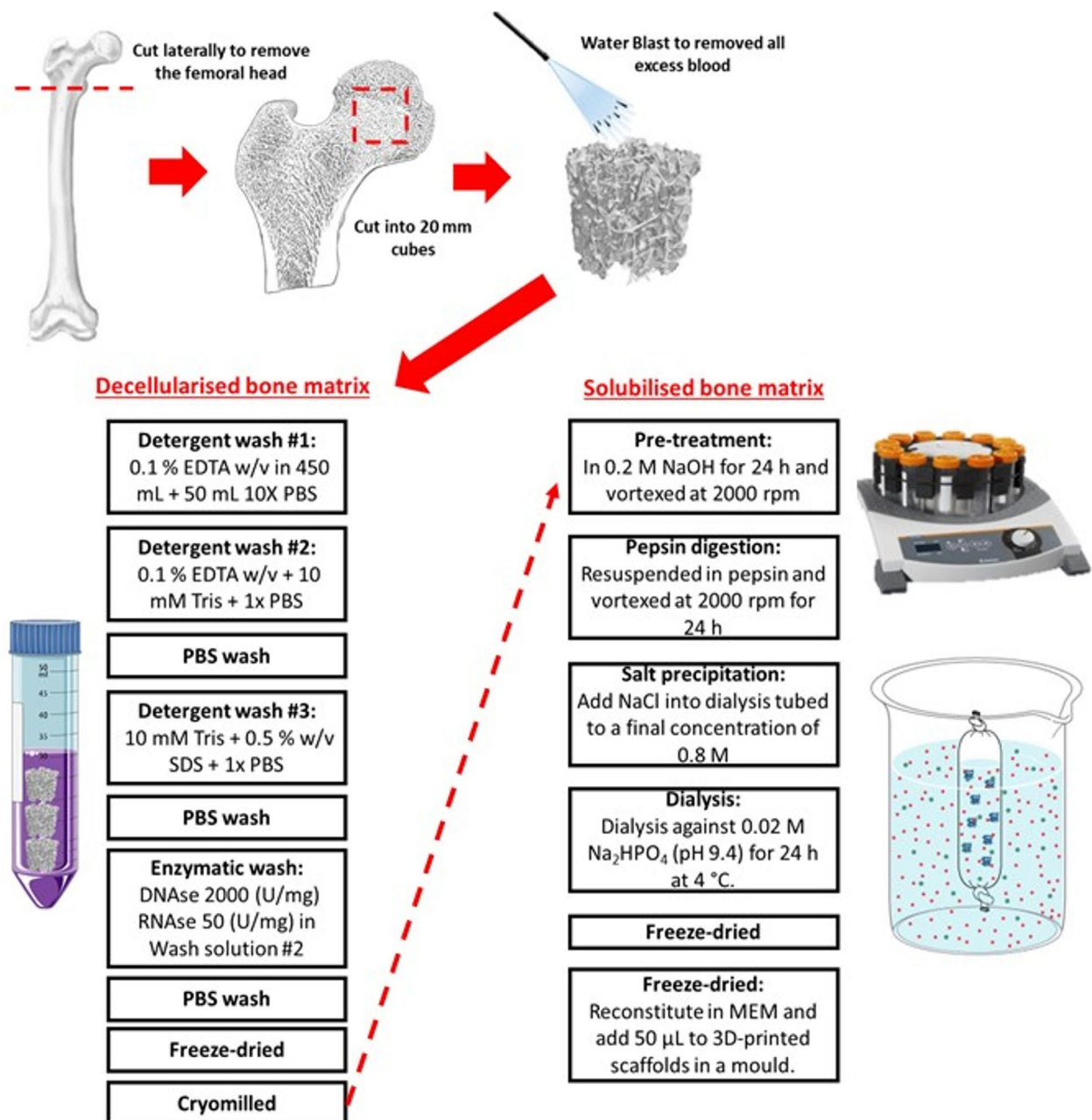


Fig. 1. Scheme of DCB and sbECM protocols.

**Table 1.** Parameters for printing the scaffolds with either PCL alone or PCL + DCB using the regenHU bioprinter.

	PCL alone	PCL+DCB
Heat of thermopolymer tank	69 °C	69 °C
Heat of thermopolymer head	72 °C	72 °C
Pressure	1 bar	5 bar
Screw speed	30 rpm	8 rpm
Feed rate (translational speed)	3 mm/s	1.5 mm/s

iT<sup>TM</sup> PicoGreen<sup>TM</sup> dsDNA Assay (BD Biosciences) and calcium assay (Calcium Assay, Stanbio Laboratories, Boerne, TX, USA) were performed on the bone ECM, according to manufacturer's protocol, to verify it had been decellularised (0 ng DNA/50 mg ECM) but not demineralised (5.45 mg calcium/50 mg ECM) (Fig. 1).

### 3D printing

A 3D bioplotter from regenHU (3D Discovery<sup>TM</sup>) was used to print all the scaffolds. DCB (30 % w/w) was added to the PCL (Capa<sup>TM</sup>, Perstop, Italy) to generate a composite thermopolymer, as is deemed optimum for printing fidelity and being sufficiently osteoinductive (Hung *et al.*, 2016; Nyberg *et al.*, 2017). The composite thermopolymer was generated by adding the powdered DCB to the PCL within the thermopolymer chamber. Then, the chamber was heated to 60 °C in order to bring the polymer to a liquid phase and, then, screw-driven pneumatic pressure was applied to the now liquid to force it out of the chamber bottom. Once fully extruded, the composite was placed back in the heated chamber and the process was repeated three times to ensure homogenous mixing of PCL and DCB. Printing parameters of both PCL alone and composite PCL/DCB are listed in Table 1. Scaffolds of 4 mm diameter and 4 mm height, with both lateral and horizontal porosity and a fibre spacing of either 1.2 (large pores) or 0.8 mm (small pores), with both PCL alone and PCL/DCB (Fig. 2), were printed using at 25G needle (Fig. 2a). This produced scaffolds that had a porosity of either 80 % (large pores) or 70 % (small pores). Using the Olympus SZX7 microscope, the fibre diameter of the scaffolds was measured to assess the printability of the composite thermopolymer as compared to PCL-alone filament. Scaffolds were sterilised by ethylene oxide prior to cell seeding.

### Mechanical testing

All mechanical tests were performed using a single column Zwick (ZwickRoell, Ulm, Germany) with a 100 kN load cell, as previously described (Olvera *et al.*, 2015). Briefly, compression tests were performed ( $n = 6$ ) using impermeable metal platens, applying a 10 % unconfined compressive strain with a ramp displacement of 1 mm/min. Next, five compressive cycles of increasing strain ( $\epsilon$ ) amplitudes from 10 to 50 % were performed to calculate the permanent deformation of the scaffolds. The Young's modulus was defined as the slope of the linear phase of the

resulting stress-strain curve during the ramp phase of the compression.

### Cell isolation, expansion and seeding

Bone-marrow-derived MSCs were obtained from the femur of a 4-month old porcine donor. Bone marrow was removed from the femoral shaft and washed in growth medium, consisting of high-glucose Dulbecco's modified Eagle medium (DMEM; Biosciences) supplemented with 10 % foetal bovine serum (FBS, Gibco), 1 % penicillin (100 U/mL) and 1 % streptomycin (100 µg/mL) (Biosciences). A homogenous suspension was achieved by trituration using a needle. The solution was centrifuged twice at 650 ×g for 5 min and, each time, the supernatant was removed. The cell pellet was triturated and the cell suspension was filtered through a 40 µm cell sieve. Following colony formation, cells were trypsinised, counted and re-plated at a density of  $5 \times 10^3/\text{cm}^2$  for a further passage. Expansion was conducted in normoxic conditions and growth medium that was changed twice weekly. Cells were used at the end of passage 3. Scaffolds were seeded with  $1 \times 10^6$  porcine MSCs in 30 µL of growth medium and allowed to adhere for 2 h before the addition of growth medium. Scaffolds were cultured in 24-well plate in 2 mL of growth medium in normoxic conditions for up to 21 d (Fig. 2b).

### Cell viability

AlamarBlue<sup>TM</sup> assay (Invitrogen), a fluorometric indicator of cell metabolic activity, was performed to determine cell viability according to the manufacturer's protocol ( $n = 4$ ). Briefly, the scaffolds were removed from the 24-well plates at day 1, 7, 14 and 21. They were washed with PBS after aspirating the medium and placed in a fresh 48-well plate, one scaffold per well. In each well, 0.9 mL of medium and 0.1 mL of AlamarBlue<sup>TM</sup> dye were added and the plate was incubated for 4 h at 37 °C in the dark. The resulting 1 mL solution was removed from the sample and the fluorescence was measured at room temperature on a plate reader (BioTeck Synergy HT) using excitation and emission wavelengths of 520 nm and 590 nm, respectively.

Cell viability was established using a live/dead assay kit (Invitrogen). Scaffolds were rinsed in sterile PBS and incubated for 1 h in phenol-free DMEM (Sigma-Aldrich) containing 2 µM calcein and 4 µM of ethidium homodimer-1 (Invitrogen). After

incubation, the constructs ( $n = 4$ ) were rinsed again in PBS and imaged with Olympus FV1000 point-scanning confocal microscope at 488 and 543 nm.

### *In vitro* biochemical and histochemical analysis

Scaffolds were prepared for either histochemical analysis or biochemical analysis. Scaffolds were washed with PBS and treated in one of the following two ways: (1) snap-frozen and stored at  $-80^{\circ}\text{C}$  for biochemical analysis; (2) fixed overnight in paraformaldehyde before being placed in PBS and refrigerated for histochemical analysis ( $n = 4$  for histological analysis and  $n = 4$  for biochemical analysis).

### DNA content

To assess DNA content for all constructs, 1 mL of papain digestion buffer [100 mM sodium phosphate buffer containing 10 mM L-cysteine (Sigma-Aldrich), 125  $\mu\text{g}/\text{mL}$  papain (Sigma-Aldrich) and 5 mM  $\text{Na}_2\text{EDTA}$  (Sigma-Aldrich) in  $\text{ddH}_2\text{O}$  at pH 6.5] was added to the scaffolds that were placed on a rotator in an oven at  $60^{\circ}\text{C}$  overnight, as previously described (Freeman *et al.*, 2013; Freeman *et al.*, 2015b; Haugh *et al.*, 2011). Once the aggregates were digested, DNA content was performed using Quant-

iT<sup>TM</sup> PicoGreen<sup>TM</sup> dsDNA Assay (BD Biosciences), with calf thymus DNA as a standard. In minimal illumination, 10  $\mu\text{L}$  of papain digest of the sample/standard were added to a 96-well plate in triplicate. To this, 190  $\mu\text{L}$  of working solution [1 $\times$  Tris-EDTA (TE) buffer and 2.5  $\mu\text{L}/\text{mL}$  Quant-iT<sup>TM</sup> PicoGreen<sup>TM</sup> dsDNA Assay solution (BD Biosciences)] were added. The plate was incubated in the dark for 5 min and, then, read using a microplate reader (BioTek Synergy HT Microplate Reader) at an excitation wavelength of 480 nm and emission of 520 nm.

### Calcium production

Calcium deposition within the scaffolds was measured using the Calcium LiquiColor<sup>®</sup> Test (Stanbio Laboratories) according to the manufacturer's protocol. Briefly, a cell lysate was prepared using 0.5 mL of Triton X-100 and 0.5 mL trichloroacetic acid. Samples were incubated for 60 min and, then, centrifuged. The supernatant was used to calculate calcium levels. Next, 10  $\mu\text{L}$  of each sample and assay standard were added to a 96-well plate and 200  $\mu\text{L}$  of the working solution were added. The plate was analysed on a microplate reader (Biotek, Synergy HT, Swindon, UK) at an absorbance of 550 nm, as previously described (Shor *et al.*, 2009). The calcium

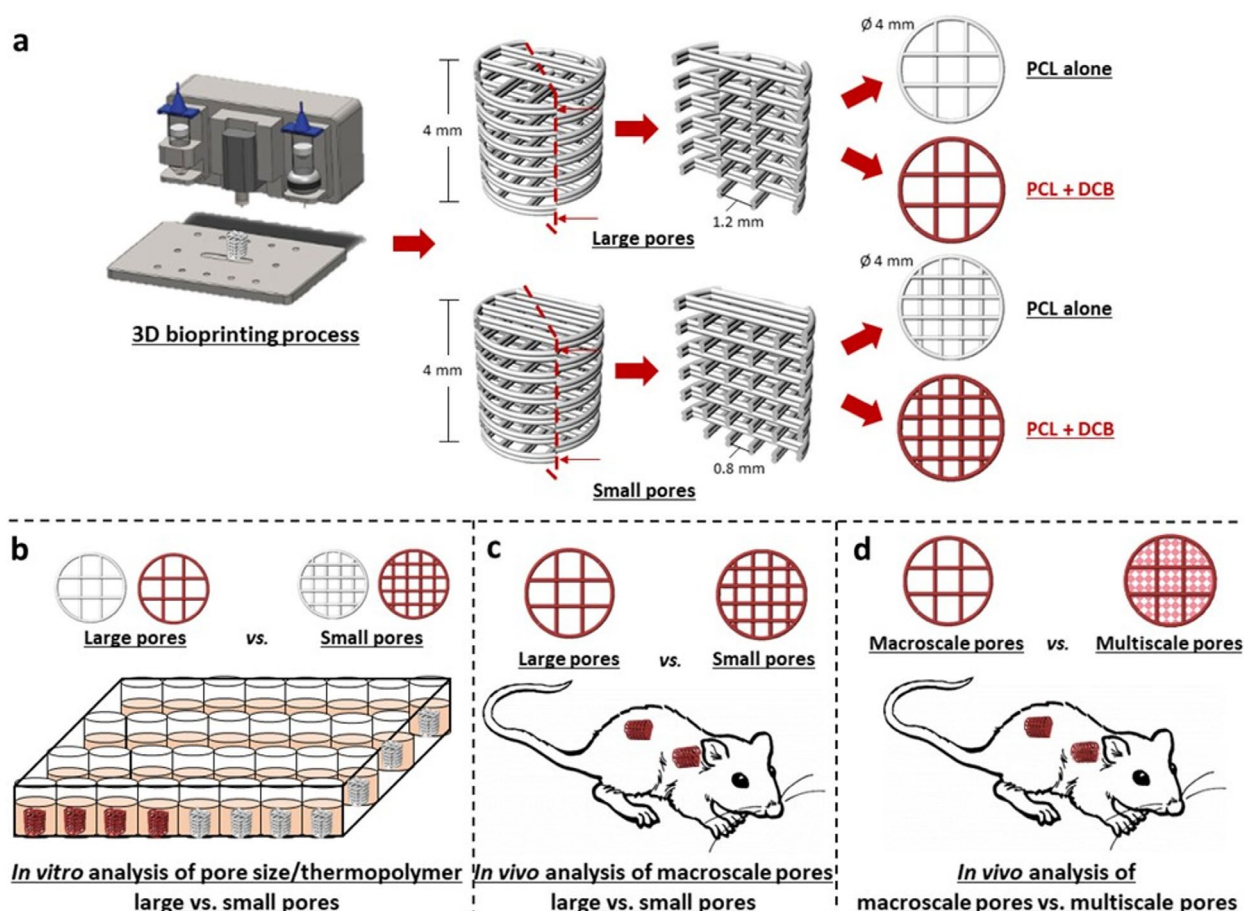


**Fig. 2. Scheme of experimental setup.** (a) Schematic representation of the 3D bioprinting process, including key geometrical features of the scaffolds printed with either PCL alone or PCL + DCB. (b) Schematic of the *in vitro* differentiation process. Schematic representation of the *in vivo* analysis of (c) macroscale pore geometries (large vs. small pores) and (d) macroscale pore only vs. multiscale pore geometries.  $\phi$ : diameter.

content at day 0 was subtracted from the reading for each sample to accommodate for the higher levels of calcium present in the scaffolds containing DCB.

#### Alizarin red staining

Samples were washed thoroughly with PBS before being stained with a 2 % alizarin red solution (Sigma-Aldrich) for 1 h. Then, they were washed thoroughly with PBS to remove any excess stain. Scaffolds were imaged using the Olympus SZX7 microscope.

#### Solubilisation procedure and scaffold design

From this point onwards, the composite thermopolymer was used to print all scaffolds. Large and small pore scaffolds were printed as described above. The large pore scaffold was also used as the backbone of the multiscale pore scaffold. Solubilised bone matrix was prepared using the aforementioned cryomilled DCB and was pre-treated with 0.2 M NaOH for 24 h and vortexed at 2,000 rpm. After removal of the pre-treatment solution, the tissue was washed in sterile dH<sub>2</sub>O. Bone ECM was subsequently solubilised using a solution of 1,500 U/mL pepsin (Sigma-Aldrich) in 0.5 M acetic acid (Sigma-Aldrich). Then, the tissue sample was vortexed again (2,000 rpm) for 24 h at room temperature to solubilise the bone. To remove insoluble material, bone ECM was centrifuged at 2,500 ×g for 1 h. Next, the supernatant containing the solubilised tissue was transferred to a new tube and combined with a 5 M NaCl (Sigma-Aldrich) solution to a final concentration of 0.8 M NaCl to preferentially salt-precipitate type I collagen (Deyl *et al.*, 2003). The salt and collagen solution was mixed followed by equilibration overnight at 4 °C. Subsequently, the solution was centrifuged at 2,500 ×g for 1 h at 4 °C. The supernatant was discarded and the collagen pellet was resuspended in 0.5 M acetic acid followed by rotation at 4 rpm overnight at room temperature to fully dissolve the collagen. Then, the salt precipitation procedure was repeated a second time. Next, the acid-solubilised collagen was transferred into dialysis membrane [molecular weight cut-off (MWCO) 6-8 kD; Spectrum Labs]. Dialysis was performed for 48 h at 4 °C using 0.02 M Na<sub>2</sub>HPO<sub>4</sub>, with agitation of the dialysate. The dialysing solution was replaced with a fresh solution after 24 h. Following dialysis, the solubilised bone solution was transferred to 24 well tissue culture plates (1 mL/well) and lyophilised. Once lyophilised, the solubilised bone ECM, hereafter known as sbECM, was stored at - 80 °C prior to scaffold fabrication.

The large pore 3D-printed scaffolds were soaked in growth medium for 2 h prior to addition of sbECM. In order to fabricate the multiscale scaffolds, lyophilised sbECM was weighed and transferred to sterile tubes. Under sterile conditions, the lyophilised sbECM was resuspended in high-glucose DMEM + Glutamax (hgDMEM; Gibco) to a final concentration of 20 mg/mL. To dissolve the sbECM, 80 µL of 0.5 M

acetic acid were added per mL of sbECM solution to a final concentration of 0.02 M acetic acid. The solution was pipetted several times to ensure homogeneous mixing. Then, the sbECM solution was brought to neutral pH by adding 20 µL of 0.1 M NaOH until the colour of the solution changed from yellow to red. Then, the sbECM solution was chemically crosslinked using glyoxal (Sigma-Aldrich) at a final concentration of 5 mM. Glyoxal is a small dialdehyde that crosslinks free amine groups in the collagen (Rao *et al.*, 2012). The solution was mixed well and incubated for 30 min at 37 °C to allow crosslinking to occur. After crosslinking, the solution was transferred to custom-made moulds (height: 5 mm; diameter: 4 mm) which contained the previously prepared PCL/DCB scaffolds. 40 µL of the crosslinked sbECM were added to each mould containing a PCL/DCB scaffold and freeze-dried (FreeZone Triad, Labconco™, Kansas City, MO, USA). To create porous scaffolds, the solution was initially frozen to - 30 °C at a rate of - 1 °C/min. This temperature was held for 1 h before rising to - 10 °C at a rate of + 1 °C/min. Once at - 10 °C, this temperature was maintained under a vacuum of 0.200 mBar for 24 h before the temperature was increased to + 20 °C at a rate of + 1 °C/min (Almeida *et al.*, 2014).

#### ECM characterisation

Solid-state nuclear magnetic resonance (ssNMR) spectroscopy experiments were conducted on a Bruker 400 MHz Avance-III spectrometer with a TopSpin software. Decellularised bone ECM was packed into a 4.0 mm (outer diameter) zirconia rotor and spun at 20 kHz in a 4 mm Bruker MAS probe. <sup>1</sup>H and <sup>13</sup>C chemical shifts were referenced to adamantane at δ(<sup>1</sup>H) = 1.85 ppm and δ(<sup>13</sup>C) = 38.52 ppm (left peak), respectively; whereas <sup>31</sup>P chemical shift was referenced to H<sub>3</sub>PO<sub>4</sub> (85 % w/w aqueous solution) at δ<sup>31</sup>P = 0.0 ppm.

Proteomic analysis was carried out as previously described (Cunniffe *et al.*, 2019). Briefly, freeze-dried solubilised bone ECM was resuspended in 0.05 M acetic acid. Precipitation of proteins was done using trichloroacetic (TCA) solution (1 : 4 volume TCA : protein), 200 µL acetone, 6 M urea in 50 mM ammonium bicarbonate (ABC) followed by treatment in 5 mM dithio-threitol (DTT) at 60 °C for 30 min, 10 mM iodoacetamide (IAA) at room temperature for 30 min and trypsin digestion prior to mass spectrometry (MS) analysis (all reagents from Sigma-Aldrich). Samples were run on a Thermo Fisher Scientific Q Exactive™ Hybrid Quadrupole-Orbitrap™ Mass Spectrometer connected to a Dionex UltiMate™ 3000 (RSLCnano, Thermo Fisher Scientific) chromatography system. Tryptic peptides were resuspended in formic acid. Each sample was loaded onto a fused silica emitter [75 µm inner diameter), pulled using a laser puller (Sutter Instruments P2000, Novato, CA, USA)], packed with UChrom C18 (1.8 µm) reverse phase media

(nanoLCMS Solutions LCC, Oroville, CA, USA) and separated by an increasing acetonitrile gradient over 45/60 min at a flow rate of 250 nL/min. The mass spectrometer was operated in positive ion mode, with a capillary temperature of 320 °C and a potential of 2,300 V applied to the frit. All data were acquired with the mass spectrometer operating in automatic data-dependent switching mode. A high resolution (70,000) MS scan (300–1600 m/z) was performed using the Q Exactive™ Hybrid Quadrupole-Orbitrap™ Mass Spectrometer to select the 8 most intense ions prior to MS/MS analysis using higher-energy collisional dissociation (HCD). Raw data were *de novo* sequenced and searched against the *sus scrofa* complete UniProt database using the search engine MaxQuant (Cox *et al.*, 2009; Tyanova *et al.*, 2016a; Zhou *et al.*, 2016) for peptides cleaved with trypsin. Each peptide used for protein identification met specific MaxQuant parameters, *i.e.* only peptide scores that corresponded to a false discovery rate (FDR) of  $\leq 1\%$  were accepted. Proteins identified by MaxQuant were processed with Perseus (Tyanova *et al.*, 2016b) to elucidate remaining proteins in solubilised bone.

### Scanning electron microscopy (SEM)

SEM was carried out on an ULTRA Plus microscope (Zeiss) operating at 5 kV accelerating voltage. Constructs were mounted on an aluminium stub using conductive carbon adhesive stickers and subsequently coated with approximately 5 nm of Au/Pd prior to imaging for 90 s at 0.1 mBar. To quantify the mean pore size of the multiscale scaffolds, 5 images (containing a minimum of 100 pores) from three different scaffolds were measured using the analyse particle function of imageJ following thresholding of the images.

### Surgical procedures

All animal procedures were ethically approved and conducted under the ethics committee of the Trinity College Dublin and the Health Products Regulatory Authority (HPRA) under protocol number AE19136/P069. Sixteen 8-week old BALB/c OlaHsd-Foxn1<sup>nu</sup> nude mice (Envigo, Oxford, UK) were anaesthetised using a mixture of xylazine (10 mg/kg) and ketamine (100 mg/kg) given subcutaneously before surgery. Once anaesthetised, 5 mg/kg carprofen was also administered subcutaneously. Two incisions were made in the skin slightly lateral to the spine of each animal and four subcutaneous pockets were created. As stated previously, scaffolds were seeded with  $1 \times 10^6$  porcine MSCs in 30  $\mu$ L of growth medium and allowed to adhere for 2 h before implantation. Large and small pore scaffolds and multiscale pore scaffolds were implanted (Fig. 2c,d). Two samples per group were put in the top two pockets with two samples from a different group in the bottom two pockets. Constructs were implanted in a balanced manner, such that each group contained an implant placed at

each of the two subcutaneous locations and samples were randomly distributed across the operated animals. Once the four constructs were implanted, incisions were closed using sutures and tissue glue.

### Micro-computed tomography ( $\mu$ CT) imaging

Prior to surgery, at 2 and 8 weeks post-surgery, scaffolds were extracted and incubated in paraformaldehyde for 24 h before being imaged using  $\mu$ CT scans on a MicroCT42 (Scanco Medical) at 55 kVp, 145  $\mu$ A and a 12  $\mu$ m voxel size. Constructs were scanned and post-processed using a threshold value that accurately depicted both the mineral content by visual inspection of the 2D greyscale tomograms (Scanco Medical MicroCT42). Noise was removed using a low-pass Gaussian filter (sigma = 1.2, support = 2). Each scaffold was normalised to  $\mu$ CT scans prior to implantation to accommodate for the different levels of mineralisation present in each scaffold.

### Histochemical analysis

Following  $\mu$ CT scanning, samples were dehydrated and embedded in paraffin-wax using an automatic tissue processor (Leica ASP300). All samples were sectioned with a thickness of 8  $\mu$ m using a rotary microtome (Leica Microtome RM2235). Sections were stained with haematoxylin and eosin (H&E) for vessel infiltration and Masson's trichrome for bone formation. Quantitative analysis was performed on multiple H&E-stained slices, whereby vessels (positive staining for endothelium and erythrocytes present within the lumen) were counted on separate sections taken throughout each construct and averaged for each construct. Masson's-trichrome-stained sections were evaluated for new bone formation. Masson's trichrome technique combines haematoxylin for cell nuclei (blue/black), fuchsin for cytoplasm, muscle and erythrocytes (red) and light green solution for collagen (green). Percentage of new bone per total area of construct was measured in separate sections using the ImageJ plugin.

### Immunofluorescence analysis

Immunofluorescence analysis was used to detect  $\alpha$ -smooth muscle actin ( $\alpha$ -SMA) and von Willebrand factor (vWF). Sections were deparaffinised overnight in an oven before undergoing a series of rehydration steps through varying ethanol grades (100–50 %). Then, samples were treated for 20 min at 37 °C with 20  $\mu$ g/mL of proteinase K, rinsed with 0.5 % (v/v) PBS-Tween 20 and blocked for 60 min at room temperature with 3 % of donkey serum, 1 % w/v BSA (w/v) in PBS (all reagents were purchased from Sigma-Aldrich). Sections were incubated overnight at 4 °C with goat polyclonal  $\alpha$ -SMA (ab21027; Abcam, 1 : 250) in PBS with 3 % donkey serum (w/v) and 1 % BSA. After three washing steps with PBS containing 1 % w/v BSA, sections were incubated with Alexa Fluor® 488 donkey anti-goat secondary

antibody (ab150129; Abcam, 1 : 200) for 1 h at room temperature in the dark. Samples were washed three times in PBS with 1 % w/v BSA and slides were incubated overnight at 4 °C with rabbit polyclonal vWF antibody (ab6994; Abcam, 1 : 200) in PBS with 3 % donkey serum (w/v) and 1 % BSA. After three washing steps with PBS and 1 % w/v BSA, sections were incubated Alexa Fluor® 647 donkey anti-rabbit secondary antibody (ab150075, Abcam, 1 : 200), for 1 h at room temperature in the dark. Finally, samples were washed three times with PBS and 1 % w/v BSA and sections were mounted using 4',6-diamidino-2-phenylindole (DAPI) mounting medium (Sigma-Aldrich). Fluorescence emission was detected using a confocal laser scanning microscopy (Olympus Fluoview FV1000).

### Statistical analysis

Results were expressed as mean  $\pm$  standard deviation. DNA content and fold change in mineral volume were examined using two-way analyses of variance (ANOVA) with the addition of Tukey's correction for multiple comparisons testing. Mechanical properties and calcium content for each scaffold were examined by one-way ANOVA with the addition of Tukey's correction for multiple comparisons testing. All other quantitative analyses were examined by an unpaired two-tailed *t*-test. All analyses were performed using GraphPad Software. For all comparisons, the level of significance was  $p \leq 0.05$ .

## Results

### The addition of DCB into PCL enhanced scaffold mechanical properties

Scaffolds with both large (filament spacing = 1.2 mm) and small (filament spacing = 0.8 mm) pores were produced by fused deposition modelling of either PCL-only or a composite of 70 % PCL and 30 % DCB. The addition of DCB into PCL significantly increased the Young's modulus of 3D-printed scaffolds with both large and small pores as compared to scaffolds printed using PCL alone (Fig. 3a). As expected, reducing the scaffold pore size significantly increased the Young's modulus of the 3D-printed scaffolds. These differences in mechanical properties were not due to thicker filaments as there was no significant difference in fibre diameter between any of the groups (Fig. 3b). There was also no significant difference in permanent deformation following the application of cyclic loading; all four scaffolds experienced a permanent deformation of approximately 30 % after cyclic loading to 50 % strain (Fig. 3c).

SEM depicted the smooth surface architecture of the PCL alone scaffolds (large and small pores) (Fig. 3d,f). In contrast, SEM revealed a rougher surface architecture with the addition of the DCB into the PCL (Fig. 3e,g).

$^1\text{H}$ ,  $^{13}\text{C}$  and  $^{31}\text{P}$  ssNMR spectra were also recorded to establish the makeup of the dECM (Fig. 7a-c). First,  $^{31}\text{P}$  ssNMR spectrum showed the presence

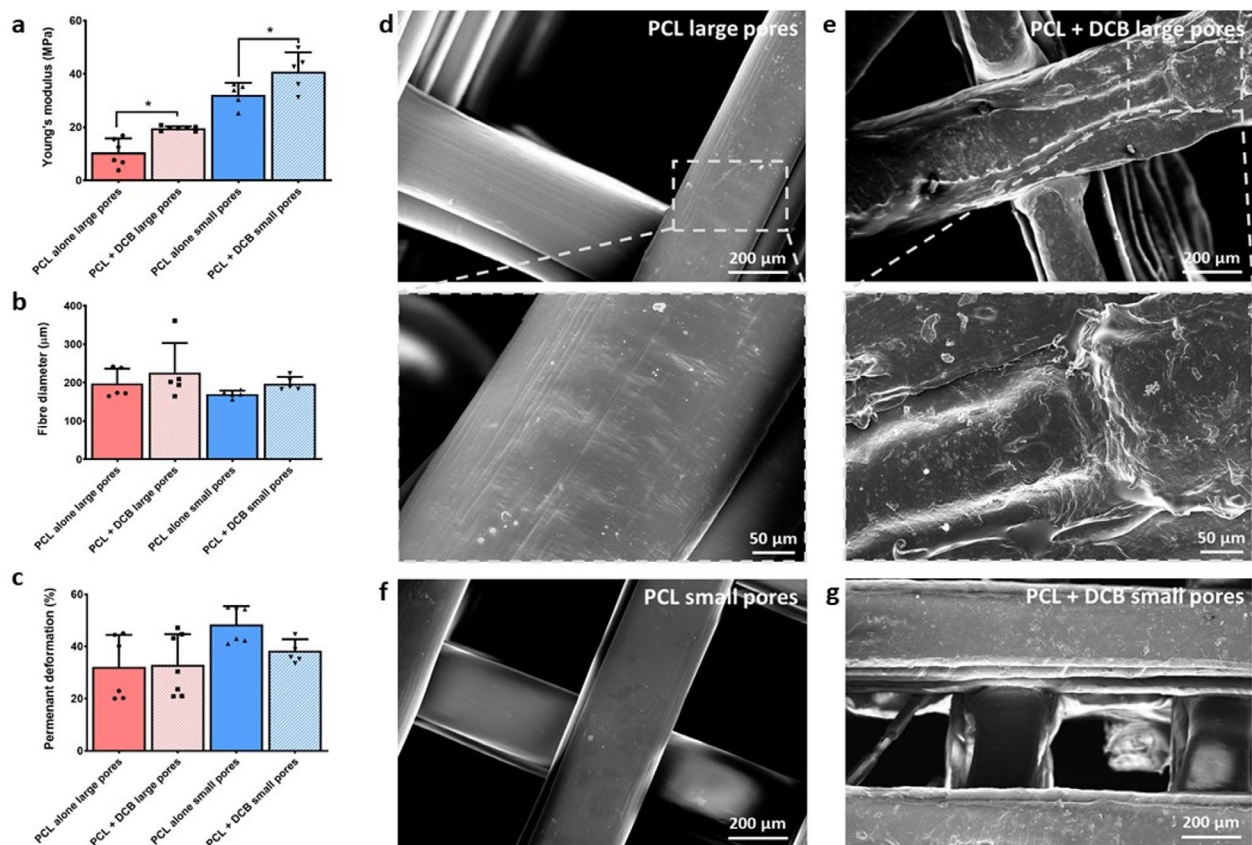


**Fig. 3. Characteristics and mechanical properties of the scaffolds.** (a) Young's modulus, (b) fibre diameter and (c) permanent deformation of both scaffold geometries printed with either PCL or PCL + DCB. Error bars denote standard deviation,  $n = 8$ , \*  $p < 0.05$ . (d-g) SEM images of all four scaffolds.

of bone mineral particles in the solubilised dECM. Indeed, dECM  $^{31}\text{P}$  signal was in the form of a single, broad [full width at half maximum (FWHM) =  $580 \pm 20$  Hz] and slightly asymmetric resonance whose maximum intensity was at  $\delta(^{31}\text{P}) = 3.2$  ppm; which is characteristic of bone HA (Von Euw *et al.*, 2019). In addition, the above-mentioned features (lineshape and linewidth) were very similar to those observed in the  $^{31}\text{P}$  ssNMR spectrum of intact bone tissue samples. This suggested that the local phosphate environments of the bone mineral particles in dECM were not altered during the decellularisation process. Second, both dECM  $^{13}\text{C}$  and  $^1\text{H}$  ssNMR spectra showed the presence of organic material. While the identification of specific proteins or other biomacromolecules was not possible, these spectra provide some compositional information since they revealed several signals attributed to different chemical groups. Among them, alkyl groups belonging to proteins and/or lipids were observable in the form of several  $^{13}\text{C}$  and  $^1\text{H}$  resonances observable in the ranges of  $\delta(^{13}\text{C}) = 10$ -65 ppm and  $\delta(^1\text{H}) = 1$ -2 ppm, respectively. In addition, aromatic and amid groups belonging to proteins were observable in the form of  $^{13}\text{C}$  resonances observable at  $\delta(^{13}\text{C}) = 130.1$  ppm and 172.0 ppm, respectively. Therefore, this demonstrated that dECM had still got most of bone inherent properties post-processing.

### Functionalisation of PCL scaffolds with DCB enhanced MSC osteogenesis *in vitro*

To assess their capacity to support osteogenesis, 3D-printed scaffolds were seeded with bone-marrow-derived MSCs and maintained in growth medium for 21 d. After 24 h of culture, there was significantly more DNA ( $352.47$  vs.  $17.1$  ng/mL;  $p = 0.0064$ ) measured in PCL + DCB large pore scaffolds as compared to PCL alone counterparts (Fig. 4a), indicating higher levels of initial cell attachment on the DCB functionalised scaffolds. There was also significantly ( $p < 0.0001$ ) more DNA in both small pore scaffolds (PCL alone:  $415.08$  ng/mL; PCL + DCB:  $529.87$  ng/mL) than in large pore PCL-alone scaffolds. There was no significant difference in DNA content between both small pore scaffolds (PCL alone, PCL + DCB). The same trend was also seen in the cellular metabolic activity after 24 h (Fig. 4b). Live/dead staining of all four groups showed viable MSCs attached to the printed filaments after 24 h (Fig. 4c).

Cell metabolic activity significantly increased over time in both large pore scaffolds (PCL alone, PCL + DCB), with less dramatic increases observed in the small pore scaffolds (Fig. 4b). DNA content significantly increased ( $p < 0.001$ ) within all scaffolds from day 1 to day 21 (Fig. 4a). At day 21, both scaffolds containing DCB (large pore:  $1268.16$  ng/mL; small pore:  $1562.96$  ng/mL) had a significantly higher DNA

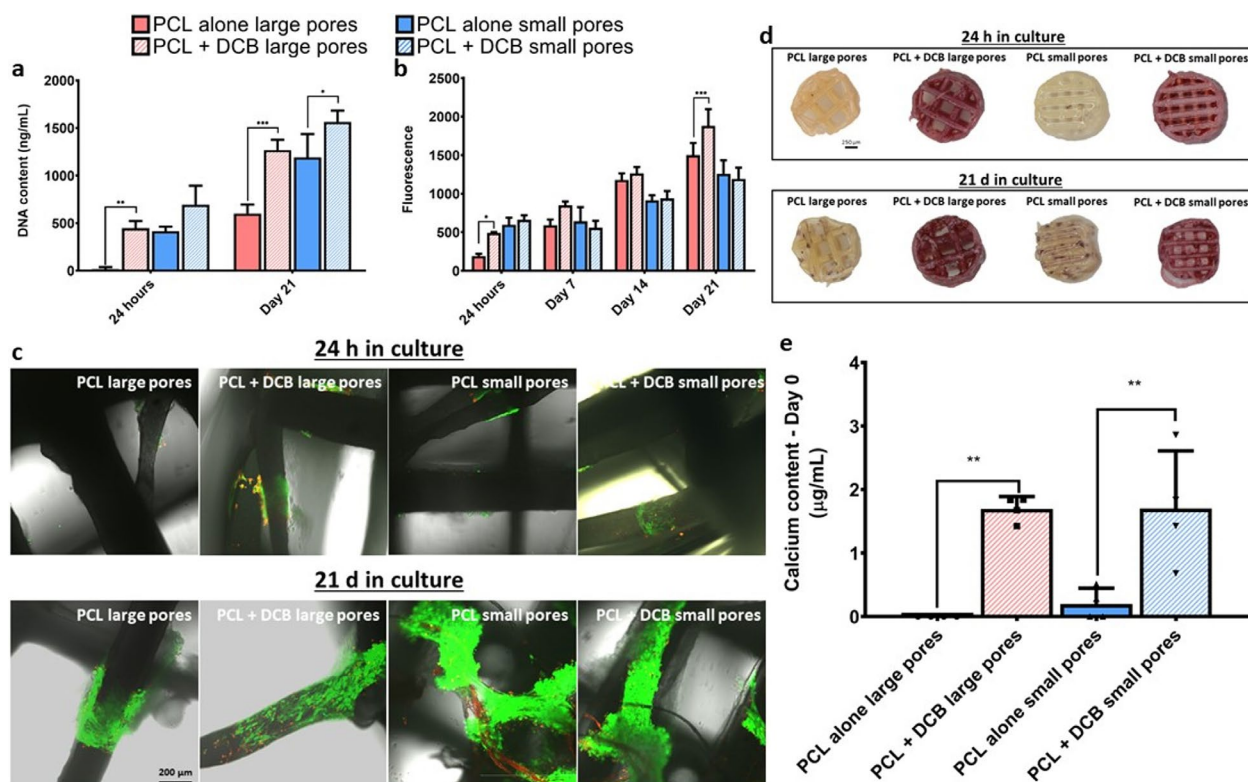


**Fig. 4. *In vitro* MSC osteogenic differentiation results.** (a) DNA content of all 4 scaffolds 24 h post MSC seeding and 21 d in culture in normoxic conditions. (b) alamarBlue™ assay of all 4 experimental groups 24 h post MSC seeding and 7, 14 and 21 d in culture in normoxic conditions. (c) Live/dead and (d) alizarin red staining of all 4 scaffolds 24 h post MSC seeding and 21 d in culture in normoxic conditions. (e) Calcium produced by all 4 scaffolds after 21 d of culture in normoxic conditions (day 0 calcium levels were subtracted from each group to account for the residual mineral content within the DCB-loaded scaffolds). \*  $p < 0.05$ , \*\*  $p < 0.01$ , \*\*\*  $p < 0.001$ . Error bars denote standard deviation,  $n = 4$ .

content than their PCL alone counterpart (large pore: 600.31 ng/mL; small pore: 1192.51 ng/mL). Live/dead staining of all four groups at day 21 showed the presence of viable MSCs present around the printed filaments (Fig. 4c).

Alizarin red staining of all four groups 24 h after seeding showed the residual positive staining present in the two scaffolds printed with PCL + DCB (large and small pore) (Fig. 4d). After 21 d in culture, a noticeable increase in positive stained mineral deposition was observed in the two scaffolds printed with PCL + DCB (large and small pore) as compared to its PCL-alone counterpart. This was further verified by measuring the increase in calcium deposition within the scaffolds over 21 d (Fig. 4e). There was significantly more calcium present in both DCB-functionalised scaffolds (large pore: 1.69  $\mu\text{g/mL}$ ; small pore: 1.84  $\mu\text{g/mL}$ ) as compared to their PCL-alone counterparts (large pore: 0  $\mu\text{g/mL}$ ; small pore: 0.19  $\mu\text{g/mL}$ ). There was no significant difference in calcium deposition between the large and small pore PCL + DCB scaffolds.

### Porosity of 3D-printed scaffolds regulated vascularisation and new bone formation *in vivo*

Having demonstrated that functionalisation of PCL with DMB enhanced osteo-inductivity of 3D-printed scaffolds *in vitro*, next, the capacity of

these composites to support vascularisation and bone formation *in vivo* was assessed. 2 weeks after subcutaneous implantation of MSC-laden scaffolds into nude mice, histological analysis of H&E-stained samples revealed the presence of vessels within both large and small pore PCL-DCB scaffolds (Fig. 5a), predominantly at the implant periphery. These vessels appeared mature, as evident by  $\alpha$ -SMA- and vWF-stained walls and vessels perfused with erythrocytes (Fig. 5a,c). When quantified, large pore scaffolds contained significantly more vessels than small pore scaffolds (Fig. 5b).

2 and 8 weeks after implantation, no significant increase in mineral volume was observed in the small pore scaffolds as compared to day 0 levels (Fig. 6a,b). In contrast, a significant 3-4 fold increase in mineral volume was measured in large pore scaffolds at both time points as compared to day 0 levels.  $\mu\text{CT}$  reconstructions revealed that mineral deposition seemed to form along the PCL + DCB filaments over the course of the study. Histological staining further verified this finding, with positive staining for new bone seen around PCL + DCB filaments (Fig. 6c, denoted by white arrows) in large pore scaffolds. Quantification revealed that large pore scaffolds had significantly more new bone (10.22 % *vs.* 5.89 %;  $p < 0.0001$ ) formation per total area of construct (Fig. 6d). Therefore, the large pore scaffold was determined

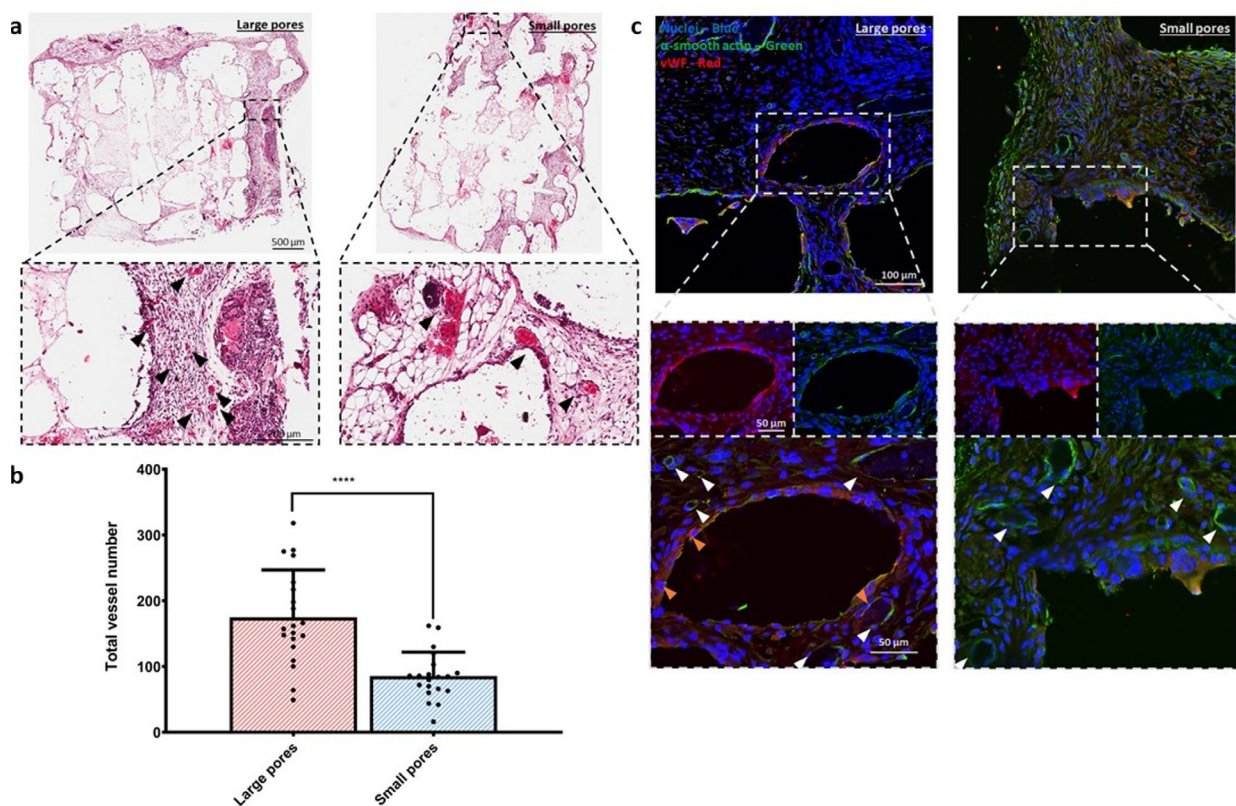


**Fig. 5. Vessel infiltration in the large and small pore scaffolds.** (a) H&E-stained sections of the two groups 2 weeks post-implantation. Black arrows denote perfused vessels complete with nuclei-stained lumen and erythrocytes. (b) Total vessel number of both groups 2 weeks post-implantation. \*\*\*\*  $p < 0.0001$ . Error bars denote standard deviation,  $n = 6$  animals,  $n = 4$  slices per animal. (c) Immunohistochemical staining of nuclei (blue), vWF (red) and  $\alpha$ -SMA (green) of both groups 2 weeks post-implantation. White arrows denote vessels with  $\alpha$ -SMA, orange arrows denote vessels with vWF.

to have the best macroscale pore geometry to support vascularisation and new bone formation. This scaffold was selected for further development and from hereon is defined as the macroscale pore scaffold.

### Multiscale bone ECM scaffolds supported enhanced cellular attachment, vessel ingrowth and new bone formation *in vivo*

Recognising that new bone generally formed on, but not between, the filaments of the 3D-printed scaffolds, a network of sbECM with microscale porosity was incorporated in between the filaments of the 3D-printed scaffold to produce a multiscale scaffold. MS analysis of the solubilised bone showed that the matrix was predominately composed of *COL1A1*, *COL1A2* with some *COL2A1* and traces of *COL9A2* (Fig. 7 and Table 2). To this end, the macroscale pore scaffolds were filled with a slurry of sbECM and the entire construct was freeze-dried. The inclusion of sbECM to produce a multiscale pore scaffold drastically increased the cellular attachment as compared to the 3D-printed scaffold with only macroscale porosity (Fig. 8a). Live/dead imaging showed that this increase in cellularity was due to cells predominantly attaching to the microporous section of the scaffolds (Fig. 8b). In contrast, in scaffolds with macroscale pores only, cells were only

found lining the PCL + DCB filament. SEM images of the multiscale pore scaffold showed the sbECM fully integrated within the PCL + DCB filament (Fig. 8c). The rough surface architecture was still observed on the PCL + DCB filament.

Next, both the macroscale and multiscale pore scaffolds were seeded with bone marrow stromal cells (BMSCs) and implanted subcutaneously into nude mice. 2 weeks after implantation, H&E staining revealed that both the macroscale and multiscale pore scaffolds had vessels present within the scaffold (Fig. 9a). They were mature blood vessels complete with  $\alpha$ -SMA- and vWF-stained walls and perfused with erythrocytes (Fig. 9a,d). Macroscale pore scaffolds had vessels predominantly located in their periphery, with little to none present in the centre. On the other hand, vessels were present both in the periphery and in the centre of the multiscale pore scaffold. When quantified, comparable numbers of vessels were observed throughout both scaffolds (Fig. 9b), however, significantly more vessels were present in the centre of the multiscale pore scaffold as compared to the macroscale pore scaffold (Fig. 9c).

Prior to implantation there was little to no difference in mineral content between the two groups as the solubilisation process used to process the DCB into a microscale scaffold removed all mineral from the ECM (Fig. 10a). Similar increases in mineral

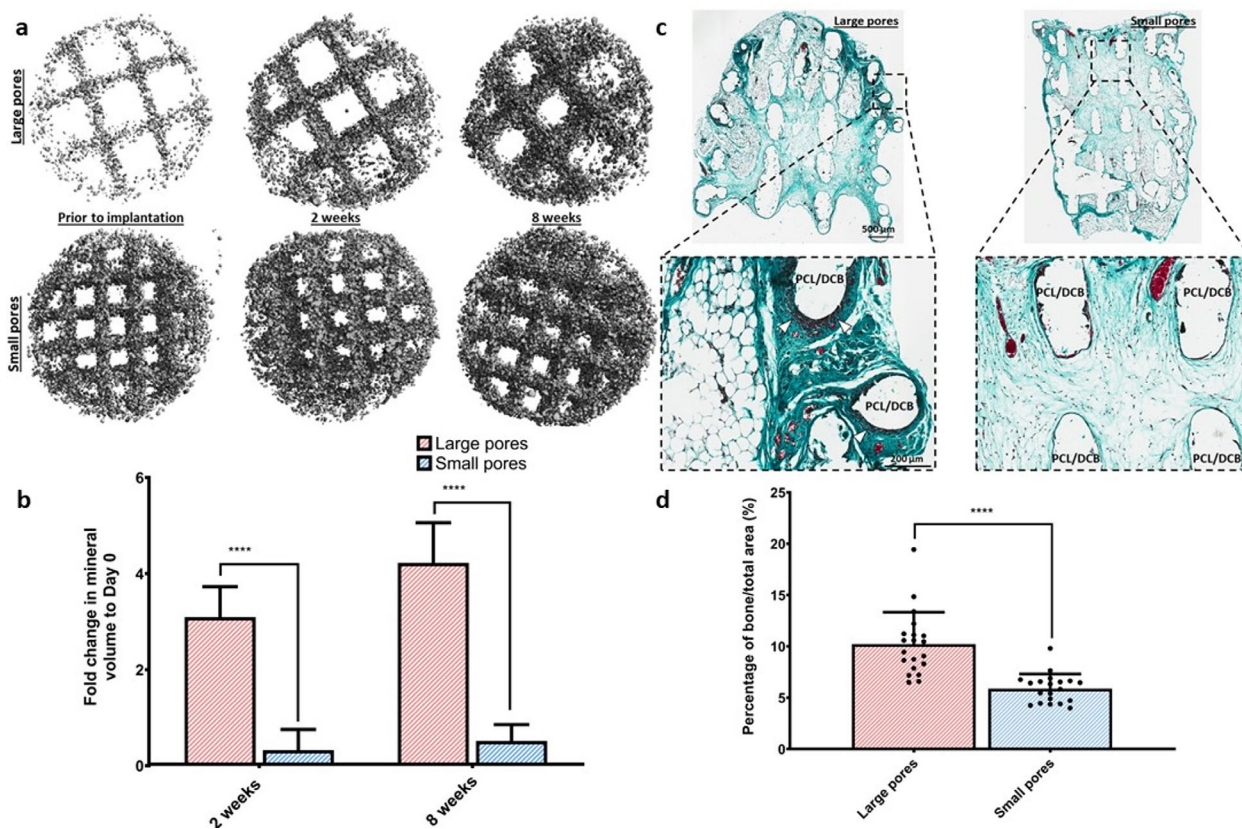


**Fig. 6. Bone formation in large and small pore scaffolds.** (a)  $\mu$ CT reconstructions of both scaffolds prior to implantation, 2 and 8 weeks post-implantation. (b) Fold change in mineral volume for its representative scaffold prior to implantation. \*\*\*\*  $p < 0.0001$ . Error bars denote standard deviation,  $n = 8$  animals. (c) Masson's trichrome for both scaffolds 8 weeks post-implantation. White arrows denote new bone formation. (d) Quantification of the amount of new bone formation per total area. \*\*\*\*  $p < 0.0001$ . Error bars denote standard deviation,  $n = 6$  animals,  $n = 4$  slices per animal.

deposition were observed in both scaffolds at 2- and 8-weeks post-implantation (Fig. 10b). As observed previously, mineralisation occurred predominately around the PCL + DCB filaments in the macroscale pore scaffold. Within the multiscale pore scaffold, large deposits of mineralised tissue were also observed between the PCL + DCB filaments, as indicated by red arrows (Fig. 10a). This was further verified by Masson's trichrome staining, which revealed new bone deposition both alongside the PCL + DCB filament but also in between the filaments (Fig. 10c). When quantified, it revealed that there was significantly more new bone deposition per total area (15.16 % *vs.* 10.22 %;  $p < 0.0001$ ) in multiscale pore scaffolds as compared to macroscale pore scaffolds (Fig. 10d).

## Discussion

Despite the tremendous potential of tissue engineering techniques for regenerating critically sized bone defects, relatively few new therapies have reached the clinic. The reasons for this are multi-faceted, from the significant cost and regulatory challenges associated with cell-based therapies to technical limitations such as cell death that can occur in these scaffolds following implantation. While some bone matrix products have made it to market, none of these

products alone is ideally suited to the treatment of mechanically loaded defects and they have mostly been used in spinal fusion or dental surgeries. This study aimed to produce a multiscale porous scaffold functionalised with bone ECM components for use in bone tissue engineering. The results from the study demonstrated that functionalising PCL with decellularised bone ECM can lead to improved mechanical properties without compromising on the printability of the construct. The addition of decellularised bone ECM to PCL increased cell attachment and led to enhanced osteogenesis of MSCs without the use of exogenous growth factors. Also, how the porosity (or filament spacing) of 3D-printed scaffolds determined their utility for bone tissue engineering was explored, demonstrating increased vessel infiltration and significantly higher levels of new bone tissue formation *in vivo* in scaffolds with large pores (filament spacing). Recognising that new bone generally formed on, but not in between, the filaments of the 3D-printed scaffolds, the implants were further modified by incorporating a network of microporous bone ECM in between their filaments to produce scaffolds with multiscale porosity. These multiscale scaffolds increased cellular attachment and, *in vivo*, supported increased vessel infiltration into the centre of the scaffolds, which in turn increased new bone formation. Taken together, a scaffold was developed that was not only mechanically competent

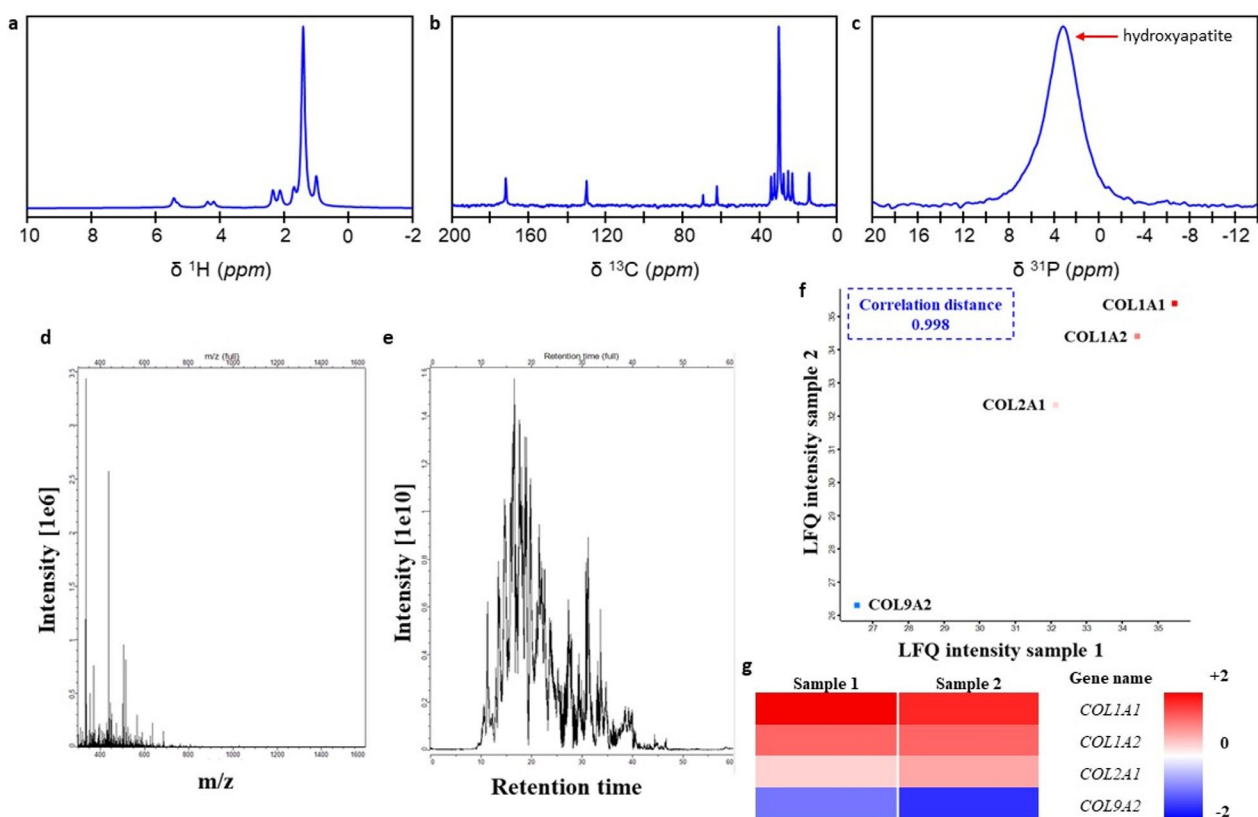


**Fig. 7. Characterisation of the ECMs.** (a)  $^1\text{H}$ , (b)  $^{13}\text{C}$  and (c)  $^{31}\text{P}$  single pulse magic angle spinning ssNMR spectra of dECM. (d) Intensity *vs.*  $m/z$  and (e) intensity *vs.* retention time graphs from MaxQuant, showing clean peaks during spectrometry analysis. (f) Scatter plot from Perseus showing label-free quantification (LfQ) intensity of bone samples, showing high correlation distance between samples. (g) Heatmap panel representing  $z$ -score of  $\log_2(\text{LfQ})$  from Table 2.

Table 2. Table of identified proteins by MaxQuant and Perseus ordered by LFQ intensity and score.

LFQ intensity 1 (Log <sub>2</sub> X)	LFQ intensity 2 (Log <sub>2</sub> X)	Peptides	Sequence coverage [%]	Molecular weight [kDa]	Score	MS/MS count	Protein IDs	Gene name
35.47463	35.39637	20	14.5	138.94	323.31	165	P02453	COL1A1
34.41602	34.41884	20	14.1	129.06	284.7	137	P02465	COL1A2
32.12546	32.33902	8	6.3	134.43	150.58	47	P02459	COL2A1
26.5529	26.30704	2	3.1	65.014	18.422	7	F1MDC2	COL9A2

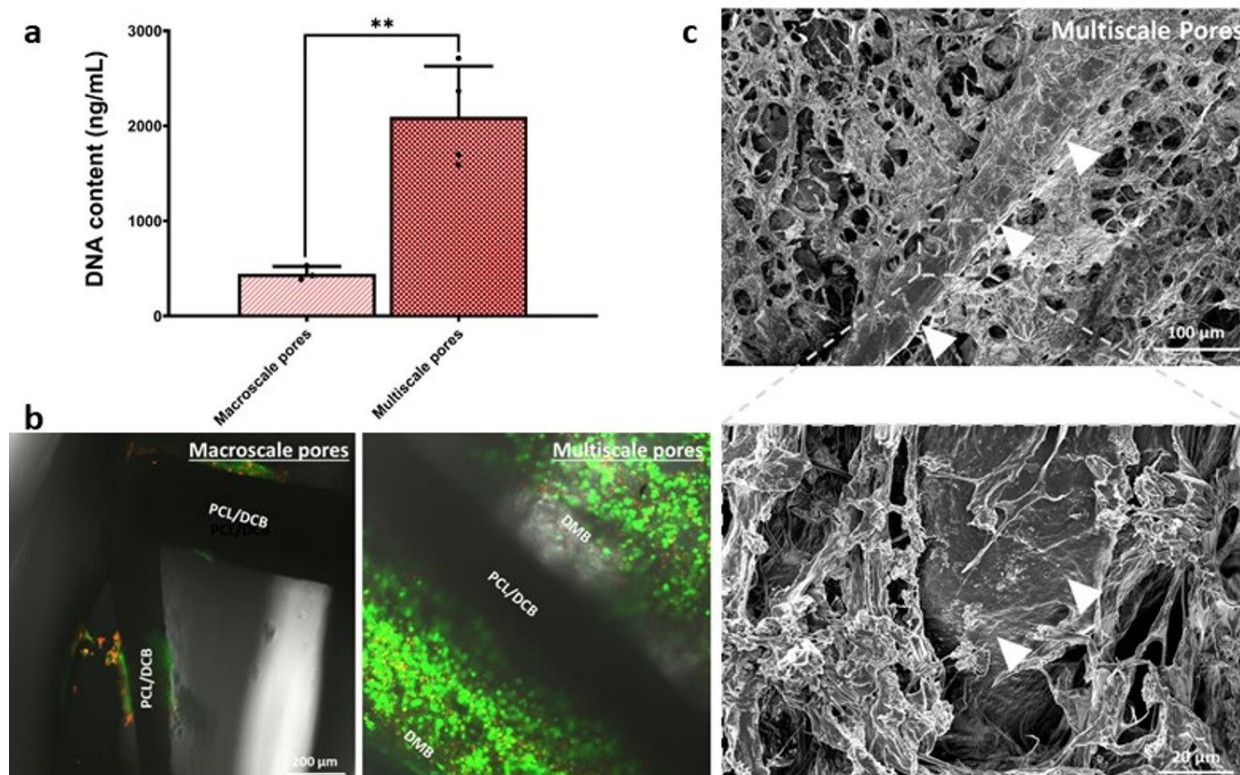


**Fig. 8.** Cellular attachment and characteristics of the multiscale porous scaffold. (a) DNA content and (b) live/dead imaging of both scaffolds 24 h post-seeding prior to implantation. Error bars denote standard deviation,  $n = 4$ ,  $** p < 0.01$ . (c) SEM images of large pore scaffold + DMB.

and porous but also provided appropriate cues to enable the osteogenic differentiation of MSCs *in vitro* and increased vascularisation and bone formation *in vivo*.

The addition of decellularised bone ECM to PCL was found to improve the mechanical properties of the resultant 3D-printed scaffolds. Interestingly, Nyberg *et al.* (2017) did not see an improvement in mechanical properties through the addition of DCB to PCL, which was contradictory to the results seen in the present study as well as previous studies reporting an improvement in mechanical properties when various forms of calcium phosphate are included into the thermopolymer (Park *et al.*, 2011; Seyednejad *et al.*, 2012; Yeo *et al.*, 2008; Yeo *et al.*, 2010). This may be due to differences in size and distribution of DCB within the PCL filaments, with Nyberg *et al.* (2017) reporting a smooth homogenous distribution of DCB

throughout the PCL filaments, whereas, within the present scaffold, the DCB was distributed throughout as small discrete nodules of DCB, as indicated by  $\mu$ CT reconstructions. The presence of these mineralised nodules did not compromise on the printability of the constructs or lead to increased fibre diameters, but their inclusion clearly increased the stiffness of the printed scaffolds. Given the differences seen in the present study, future studies will investigate the addition of higher concentrations of DCB to the PCL, at least to the point that the thermopolymer is still printable. Higher concentrations of DCB would likely further improve the osteogenic inductivity of the scaffolds whilst further improving its mechanical properties.

Addition of DCB to PCL filaments increased the osteo-inductivity of the resulting scaffold. Previous studies incorporating calcium phosphates into

3D-printed polymers have reported similar findings (Causa *et al.*, 2006; Nyberg *et al.*, 2017; Park *et al.*, 2011; Polini *et al.*, 2011; Rai *et al.*, 2010). The presence of DCB within the PCL filaments resulted in a significant increase in MSC attachment and scaffold mineralisation (a late stage osteogenic marker), without the use of any exogenous growth factor. This could be due to change in surface topography (Faia-Torres *et al.*, 2015; Kiang *et al.*, 2013; Marletta *et al.*, 2007; Olivares-Navarrete *et al.*, 2010; You *et al.*, 2010; Zhao *et al.*, 2012) with the addition of DCB, as seen in SEM images, or due to the release of calcium ions from the filaments (Aquino-Martinez *et al.*, 2017a; Aquino-Martinez *et al.*, 2017b; Liu *et al.*, 2009; Samavedi *et al.*, 2013). Future work should delve further into understanding the type and functionality of any residual growth factors present within both the decellularised bone ECM and the solubilised bone ECM as well as testing the mineralisation potential of the scaffolds using distinct MSC donors (*e.g.* male, female, age).

Due to the highly porous nature of the scaffold design, the seeding efficiency of the proposed scaffold was still rather low, with a seeding efficiency of approximately 13 % and 18 % for large and small pore scaffolds, respectively. To overcome this limitation, micro-porous solubilised bone ECM was

incorporated in between the PCL + DCB filaments to produce a multiscale bone ECM scaffold, therefore maintaining the mechanical properties of the PCL + DCB-printed scaffold but also increasing its seeding efficiency. The addition of the solubilised ECM drastically increased the seeding efficiency of the scaffold from 13 to 50 %. Due to the freeze-drying process, the mechanical properties of the scaffold did significantly deteriorate (data not shown), however, it was still in and around that typically reported for the mechanical properties of low-density trabecular bone (Goldstein, 1987).

Results showed that a 10 % change in porosity could significantly influence vascularisation of 3D-printed constructs. Both large and small pore scaffolds were vascularised after 2 weeks *in vivo*; however, there were significantly more vessels present in the large pore scaffold and, in both groups, vessels were predominantly present in the periphery of the scaffolds. Interestingly, when solubilised bone ECM was added to the large pore scaffold, it did not impede the influx of vessels within the scaffold; in fact, it actually facilitated the migration of blood vessels into the centre of the constructs. This may be due, at least in part, to increased attachment of MSCs to these scaffolds prior to implantation, as previous studies have demonstrated that MSCs can

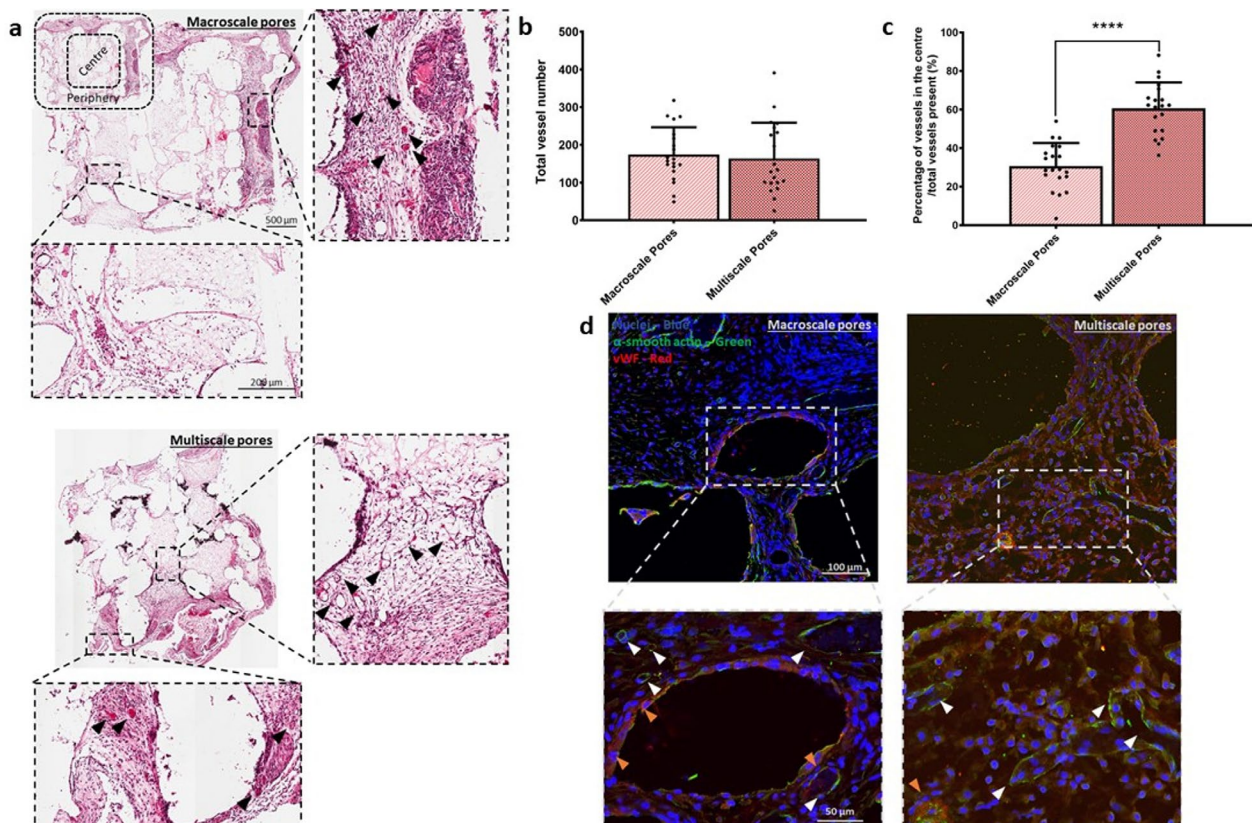


**Fig. 9. Vessel infiltration of macroscale pores versus multiscale pores.** (a) H&E-stained sections of the two groups 2 weeks post-implantation. Black arrows denote perfused vessels complete with nuclei-stained lumen and erythrocytes. (b) Total vessel number of both groups 2 weeks post-implantation. (c) Percentage of vessels present within the centre of the scaffold versus total number of vessels. \*\*\*\*  $p < 0.0001$ . Error bars denote standard deviation,  $n = 8$  animals,  $n = 4$  slices per animal. (d) Immunohistochemical staining of nuclei (blue), vWF (red) and  $\alpha$ -SMA (green) of both groups 2 weeks post-implantation. White arrows denote vessels with  $\alpha$ -SMA, orange arrows denote vessels with vWF.

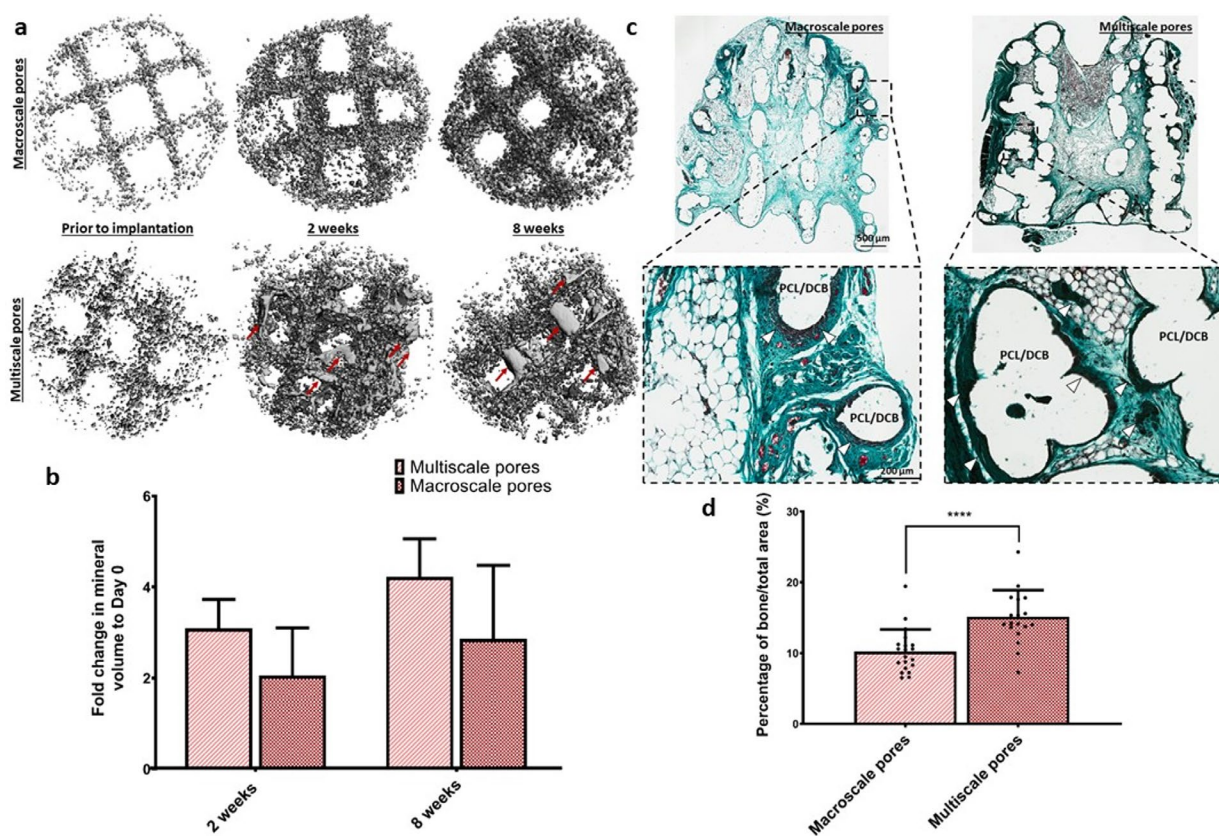


**Fig. 10. Bone formation of macroscale pores versus multiscale pores.** (a)  $\mu$ CT reconstructions of both scaffolds prior to implantation, 2 and 8 weeks post-implantation. Red arrows denote clusters of mineralisation nodules present in between the PCL + DCB filaments. (b) Fold change in mineral volume for its representative scaffold prior to implantation. Error bars denote standard deviation,  $n = 8$  animals. (c) Masson's trichrome for both scaffolds 8 weeks post-implantation. White arrows denote new bone formation. (d) Quantification of the amount of new bone formation per total area. \*\*\*\*  $p < 0.0001$ . Error bars denote standard deviation,  $n = 8$  animals,  $n = 4$  slices per animal.

secrete a range of factors that promote angiogenesis (Kusumbe *et al.*, 2014; Liu and Castillo, 2018; Liu *et al.*, 2016; Schipani *et al.*, 2009; Wang *et al.*, 2007; Yang *et al.*, 2013). The presence of the solubilised bone ECM itself was also likely contributing to this increased vessel infiltration, as previous studies have shown rapid vascularisation during demineralised bone matrix-induced osteogenesis *in vivo* (Rabie, 1997). Increased vascular invasion of bone defects was associated with an influx of macrophages, which are known to produce pro-angiogenic factors, 7 d post-implantation (Rabie, 1997). Future studies will implant bone ECM functionalised scaffolds in bone defects in fully immuno-competent animals to better elucidate the role of the immune system in scaffold-mediated bone regeneration.

Increased vascularisation correlates with increased bone regeneration (Correia *et al.*, 2011; Duffy *et al.*, 2011; Freeman *et al.*, 2015a; Freeman *et al.*, 2015b; Ghanaati *et al.*, 2011; McFadden *et al.*, 2013; Pedersen *et al.*, 2013; Rabie, 1997; Scherberich *et al.*, 2007). The results from the present study were no different: the reduction in vessel influx in the small pore scaffold also led to a significant reduction in both mineral deposition and amount of new bone formed within the 3D-printed construct. Reducing the porosity by

only 10 % can significantly affect the bone-forming potential of a 3D-printed construct. Other studies have reported similar findings with a poly(l-lactide-co-d,l-lactide) containing 20 wt %  $\beta$ -tricalcium phosphate scaffold. By increasing the porosity by only 8 % (80-88 %), Roy *et al.* (2003) observed more tissue ingrowth and new bone formation after implantation into the rabbit cranium. Together, these findings demonstrated the importance of carefully tailoring the porosity of 3D-printed scaffolds to ensure they not only facilitate high levels of cellular attachment, but also vascular invasion and new tissue deposition *in vivo*. This can be difficult to achieve using a single biofabrication strategy (*e.g.* fused deposition modelling) to produce a functional scaffold and motivates the integration of distinct approaches, such as that adopted in the present study, to produce multiscale scaffolds that can potentially promote superior regeneration as compared to the use of either biofabrication strategy alone.

## Conclusions

Appropriately engineered scaffold porosity is integral to the success of numerous tissue engineering

strategies, as without it nutrient, cell and vessel infiltration cannot occur, ultimately leading to implant failure. The present study described the development of novel bone-ECM-based scaffolds for bone tissue engineering that were designed to enhance angiogenesis and provide stem cells with the necessary cues to undergo osteogenic differentiation following implantation. Macro-porosity of a 3D-printed scaffold significantly influenced both vessel infiltration and bone formation *in vivo*. Furthermore, a multiscale porous scaffold could further enhance cellular attachment, vessel infiltration and bone formation *in vivo*. In summary, a scaffold was developed that was not only mechanically competent and porous on multiple scales but also provided appropriate cues to enable osteogenic differentiation of MSCs *in vitro* and enhanced vessel infiltration and bone formation *in vivo*.

### Acknowledgements

This publication was supported by a research grant from the European Research Council (ERC) under the grant number 647004 and the Irish Research Council (GOIPD/2016/324). SVE was supported by the European Union's Horizon 2020 research and innovation program under the Marie Skłodowska-Curie grant agreement No 793861.

Authors declare that no competing financial interests exist.

### References

- Almeida HV, Liu Y, Cunniffe GM, Mulhall KJ, Matsiko A, Buckley CT, O'Brien FJ, Kelly DJ (2014) Controlled release of transforming growth factor- $\beta$ 3 from cartilage-extra-cellular-matrix-derived scaffolds to promote chondrogenesis of human-joint-tissue-derived stem cells. *Acta Biomater* **10**: 4400-4409.
- Amini AR, Laurencin CT, Nukavarapu SP (2012) Bone tissue engineering: recent advances and challenges. *Crit Rev Biomed Eng* **40**: 363-408.
- Aquino-Martinez R, Angelo AP, Pujol FV (2017a) Calcium-containing scaffolds induce bone regeneration by regulating mesenchymal stem cell differentiation and migration. *Stem Cell Res Ther* **8**: 265. DOI: 10.1186/s13287-017-0713-0.
- Aquino-Martinez R, Artigas N, Gamez B, Rosa JL, Ventura F (2017b) Extracellular calcium promotes bone formation from bone marrow mesenchymal stem cells by amplifying the effects of BMP-2 on SMAD signalling. *PLoS One* **12**: e0178158. DOI: 10.1371/journal.pone.0178158.
- Cao H, Kuboyama N (2010) A biodegradable porous composite scaffold of PGA/beta-TCP for bone tissue engineering. *Bone* **46**: 386-395.
- Causa F, Netti PA, Ambrosio L, Ciapetti G, Baldini N, Pagani S, Martini D, Giunti A (2006) Poly-epsilon-caprolactone/hydroxyapatite composites for bone regeneration: *in vitro* characterization and human osteoblast response. *J Biomed Mater Res A* **76**: 151-162.
- Cheng CW, Solorio LD, Alsberg E (2014) Decellularized tissue and cell-derived extracellular matrices as scaffolds for orthopaedic tissue engineering. *Biotechnol Adv* **32**: 462-484.
- Correia C, Grayson WL, Park M, Hutton D, Zhou B, Guo XE, Niklason L, Sousa RA, Reis RL, Vunjak-Novakovic G (2011) *In vitro* model of vascularized bone: synergizing vascular development and osteogenesis. *PLoS One* **6**: 28352. DOI: 10.1371/journal.pone.0028352.
- Cox J, Matic I, Hilger M, Nagaraj N, Selbach M, Olsen JV, Mann M (2009) A practical guide to the MaxQuant computational platform for SILAC-based quantitative proteomics. *Nature Protocols* **4**: 698-705.
- Cunniffe GM, Diaz-Payno PJ, Sheehy EJ, Critchley SE, Almeida HV, Pitacco P, Carroll SF, Mahon OR, Dunne A, Levingstone TJ, Moran CJ, Brady RT, O'Brien FJ, Brama PAJ, Kelly DJ (2019) Tissue-specific extracellular matrix scaffolds for the regeneration of spatially complex musculoskeletal tissues. *Biomaterials* **188**: 63-73.
- d' Aquino R, De Rosa A, Lanza V, Tirino V, Laino L, Graziano A, Desiderio V, Laino G, Papaccio G (2009) Human mandible bone defect repair by the grafting of dental pulp stem/progenitor cells and collagen sponge biocomplexes. *Eur Cell Mater* **18**: 75-83.
- Daly AC, Cunniffe GM, Sathy BN, Jeon O, Alsberg E, Kelly DJ (2016) 3D bioprinting of developmentally inspired templates for whole bone organ engineering. *Adv Healthc Mater* **5**: 2353-2362.
- De Santis R, Gloria A, Russo T, D'Amora U, Zeppetelli S, Dionigi C, Sytcheva A, Herrmannsdorfer T, Dediu V, Ambrosio L (2011) A basic approach toward the development of nanocomposite magnetic scaffolds for advanced bone tissue engineering. *J Appl Polym Sci* **122**: 3599-3605.
- Deyl Z, Mikšik I, Eckhardt A (2003) Preparative procedures and purity assessment of collagen proteins. *J Chromatogr B Analyt Technol Biomed Life Sci* **790**: 245-275.
- Drosos GI, Kazakos KI, Kouzoumpasis P, Verettas DA (2007) Safety and efficacy of commercially available demineralised bone matrix preparations: a critical review of clinical studies. *Injury* **38**: S13-S21.
- Duffy GP, McFadden TM, Byrne EM, Gill SL, Farrell E, O'Brien FJ (2011) Towards *in vitro* vascularisation of collagen-GAG scaffolds. *Eur Cell Mater* **21**: 15-30.
- Faia-Torres AB, Charnley M, Goren T, Guimond-Lischer S, Rottmar M, Maniura-Weber K, Spencer ND, Reis RL, Textor M, Neves NM (2015) Osteogenic differentiation of human mesenchymal stem cells in the absence of osteogenic supplements: a surface-roughness gradient study. *Acta Biomater* **28**: 64-75.
- Freeman FE, Allen AB, Stevens HY, Guldberg RE, McNamara LM (2015a) Effects of *in vitro* endochondral priming and pre-vascularisation of human MSC cellular aggregates *in vivo*. *Stem Cell Res Ther* **6**: 218. DOI: 10.1186/s13287-015-0210-2.

- Freeman FE, Haugh MG, McNamara LM (2013) Investigation of the optimal timing for chondrogenic priming of MSCs to enhance osteogenic differentiation *in vitro* as a bone tissue engineering strategy. *J Tissue Eng Regen Med* **10**: E250-262.
- Freeman FE, Haugh MG, McNamara L (2015b) An *in vitro* bone tissue regeneration strategy combining chondrogenic and vascular priming enhances the mineralisation potential of MSCs *in vitro* whilst also allowing for vessel formation. *Tissue Eng Part A* **21**: 1320-1332.
- Ge Z, Tian X, Heng BC, Fan V, Yeo JF, Cao T (2009a) Histological evaluation of osteogenesis of 3D-printed poly-lactic-co-glycolic acid (PLGA) scaffolds in a rabbit model. *Biomed Mater* **4**: 021001. DOI: 10.1088/1748-6041/4/2/021001.
- Ge ZG, Wang LS, Heng BC, Tian XF, Lu K, Fan VTW, Yeo JF, Cao T, Tan E (2009b) Proliferation and differentiation of human osteoblasts within 3D printed poly-lactic-co-glycolic acid scaffolds. *J Biomater Appl* **23**: 533-547.
- Ghanaati S, Fuchs S, Webber MJ, Orth C, Barbeck M, Gomes ME, Reis RL, Kirkpatrick CJ (2011) Rapid vascularization of starch-poly(caprolactone) *in vivo* by outgrowth endothelial cells in co-culture with primary osteoblasts. *J Tissue Eng Regen Med* **5**: 136-143.
- Goldstein SA (1987) The mechanical properties of trabecular bone: dependence on anatomic location and function. *J Biomech* **20**: 1055-1061.
- Gruskin E, Doll BA, Futrell FW, Schmitz JP, Hollinger JO (2012) Demineralized bone matrix in bone repair: history and use. *Adv Drug Deliv Rev* **64**: 1063-1077.
- Guarino V, Causa F, Netti PA, Ciapetti G, Pagani S, Martini D, Baldini N, Ambrosio L (2008) The role of hydroxyapatite as solid signal on performance of PCL porous scaffolds for bone tissue regeneration. *J Biomed Mater Res B Appl Biomater* **86B**: 548-557.
- Guo T, Holzberg TR, Lim CG, Gao F, Gargava A, Trachtenberg JE, Mikos AG, Fisher JP (2017) 3D printing PLGA: a quantitative examination of the effects of polymer composition and printing parameters on print resolution. *Biofabrication* **9**: 024101. DOI: 10.1088/1758-5090/aa6370.
- Habibovic P, Gbureck U, Doillon CJ, Bassett DC, van Blitterswijk CA, Barralet JE (2008) Osteoconduction and osteoinduction of low-temperature 3D printed bioceramic implants. *Biomaterials* **29**: 944-953.
- Haugh MG, Meyer EG, Thorpe SD, Vinardell T, Duffy GP, Kelly DJ (2011) Temporal and spatial changes in cartilage-matrix-specific gene expression in mesenchymal stem cells in response to dynamic compression. *Tissue Eng Part A* **17**: 3085-3093.
- Heo SJ, Kim SE, Wei J, Kim DH, Hyun YT, Yun HS, Kim HK, Yoon TR, Kim SH, Park SA, Shin JW, Shin JW (2009) *In vitro* and animal study of novel nano-hydroxyapatite/poly(epsilon-caprolactone) composite scaffolds fabricated by layer manufacturing process. *Tissue Eng Part A* **15**: 977-989.
- Hibi H, Yamada Y, Ueda M, Endo Y (2006) Alveolar cleft osteoplasty using tissue-engineered osteogenic material. *Int J Oral Maxillofac Surg* **35**: 551-555.
- Hung BP, Naved BA, Nyberg EL, Dias M, Holmes CA, Elisseeff JH, Dorafshar AH, Grayson WL (2016) Three-dimensional printing of bone extracellular matrix for craniofacial regeneration. *ACS Biomater Sci Eng* **2**: 1806-1816.
- Hutmacher DW (2000) Scaffolds in tissue engineering bone and cartilage. *Biomaterials* **21**: 2529-2543.
- Jones AC, Arns CH, Sheppard AP, Hutmacher DW, Milthorpe BK, Knackstedt MA (2007) Assessment of bone ingrowth into porous biomaterials using MICRO-CT. *Biomaterials* **28**: 2491-2504.
- Kang HW, Lee SJ, Ko IK, Kengla C, Yoo JJ, Atala A (2016) A 3D bioprinting system to produce human-scale tissue constructs with structural integrity. *Nat Biotechnol* **34**: 312-319.
- Karageorgiou V, Kaplan D (2005) Porosity of 3D biomaterial scaffolds and osteogenesis. *Biomaterials* **26**: 5474-5491.
- Kiang JD, Wen JH, del Alamo JC, Engler AJ (2013) Dynamic and reversible surface topography influences cell morphology. *J Biomed Mater Res A* **101**: 2313-2321.
- Kim GH, Son JG (2009) 3D polycaprolactone (PCL) scaffold with hierarchical structure fabricated by a piezoelectric transducer (PZT)-assisted bioplotter. *Applied Physics A* **94**: 781-785.
- Kim J, McBride S, Tellis B, Alvarez-Urena P, Song YH, Dean DD, Sylvia VL, Elgandy H, Ong J, Hollinger JO (2012) Rapid-prototyped PLGA/beta-TCP/hydroxyapatite nanocomposite scaffolds in a rabbit femoral defect model. *Biofabrication* **4**: 025003. DOI: 10.1088/1758-5082/4/2/025003.
- Ko HC, Milthorpe BK, McFarland CD (2007) Engineering thick tissues – the vascularisation problem. *Eur Cell Mater* **14**: 1-19.
- Krecic-Stres H, Krkovic M, Koder J, Malicev E, Drobnic M, Marolt D, Kregar-Velikonja N (2007) Mesenchymal stem cells: a modern approach to treat long bones defects. In: 11th Mediterranean Conference on Medical and Biological Engineering and Computing 2007. Editors: Jarm T, Kramar P, Anze Z. **16**: 253-256.
- Kucharska M, Butruk B, Walenko K, Brynk T, Ciach T (2012) Fabrication of *in-situ* foamed chitosan/beta-TCP scaffolds for bone tissue engineering application. *Mater Lett* **85**: 124-127.
- Kusumbe AP, Ramasamy SK, Adams RH (2014) Coupling of angiogenesis and osteogenesis by a specific vessel subtype in bone. *Nature* **507**: 323-328.
- Lee J, Sung H-M, Jang J-D, Park Y-W, Min S-K, Kim E-C (2010) Successful reconstruction of 15-cm segmental defects by bone marrow stem cells and resected autogenous bone graft in central hemangioma. *J Oral Maxillofac Surg* **68**: 188-194.
- Liu C, Castillo AB (2018) Targeting osteogenesis-angiogenesis coupling for bone repair. *J Am Acad Orthop Surg* **26**: E153-E155.

- Liu C, Cui X, Ackermann TM, Flamini V, Chen WQ, Castillo AB (2016) Osteoblast-derived paracrine factors regulate angiogenesis in response to mechanical stimulation. *Integr Biol (Camb)* **8**: 785-794.
- Liu YK, Lu QZ, Pei R, Ji HJ, Zhou GS, Zhao XL, Tang RK, Zhang M (2009) The effect of extracellular calcium and inorganic phosphate on the growth and osteogenic differentiation of mesenchymal stem cells *in vitro*: implication for bone tissue engineering. *Biomed Mater* **4**: 025004. DOI: 10.1088/1748-6041/4/2/025004.
- Lyons FG, Al-Munajjed AA, Kieran SM, Toner ME, Murphy CM, Duffy GP, O'Brien FJ (2010) The healing of bony defects by cell-free collagen-based scaffolds compared to stem cell-seeded tissue engineered constructs. *Biomaterials* **31**: 9232-9243.
- Marcacci M, Kon E, Moukhachev V, Lavroukov A, Kutepov S, Quarto R, Mastrogiacomo M, Cancedda R (2007) Stem cells associated with macroporous bioceramics for long bone repair: 6-to 7-year outcome of a pilot clinical study. *Tissue Eng* **13**: 947-955.
- Marletta G, Ciapetti G, Satriano C, Perut F, Salerno M, Baldini N (2007) Improved osteogenic differentiation of human marrow stromal cells cultured on ion-induced chemically structured poly- $\epsilon$ -caprolactone. *Biomaterials* **28**: 1132-1140.
- McFadden TM, Duffy GP, Allen AB, Stevens HY, Schwarzmaier SM, Plesnila N, Murphy JM, Barry FP, Guldberg RE, O'Brien FJ (2013) The delayed addition of human mesenchymal stem cells to preformed endothelial cell networks results in functional vascularization of a collagen-glycosaminoglycan scaffold *in vivo*. *Acta Biomater* **9**: 9303-9316.
- Meijer GJ, de Bruijn JD, Koole R, van Blitterswijk CA (2007) Cell-based bone tissue engineering. *PLoS Med* **4**: 9. DOI: 10.1371/journal.pmed.0040009.
- Meijer GJ, de Bruijn JD, Koole R, van Blitterswijk CA (2008) Cell based bone tissue engineering in jaw defects. *Biomaterials* **29**: 3053-3061.
- Müller B, Deyhle H, Fierz FC, Irsen SH, Yoon JY, Mushkolaj S, Boss O, Vorndran E, Gburek U, Degistirici Ö, Thie M, Leukers B, Beckmann F, Witte F (2009) Bio-mimetic hollow scaffolds for long bone replacement. *Biomimetics and Bioinspiration* **7401**: 74010D.
- Nyberg E, Rindone A, Dorafshar AH, Grayson WL (2017) Comparison of 3D-printed poly- $\epsilon$ -caprolactone scaffolds functionalized with tricalcium phosphate, hydroxyapatite, bio-oss, or decellularized bone matrix. *Tissue Eng Part A* **23**: 503-514.
- O'Brien FJ (2011) Biomaterials & scaffolds for tissue engineering. *Materials Today* **14**: 88-95.
- Olivares-Navarrete R, Hyzy SL, Hutton DL, Erdman CP, Wieland M, Boyan BD, Schwartz Z (2010) Direct and indirect effects of microstructured titanium substrates on the induction of mesenchymal stem cell differentiation towards the osteoblast lineage. *Biomaterials* **31**: 2728-2735.
- Olvera D, Daly A, Kelly DJ (2015) Mechanical testing of cartilage constructs. *Methods Mol Biol* **1340**: 279-287.
- Park SA, Lee SH, Kim WD (2011) Fabrication of porous polycaprolactone/hydroxyapatite (PCL/HA) blend scaffolds using a 3D plotting system for bone tissue engineering. *Bioprocess Biosyst Eng* **34**: 505-513.
- Park SH, Park DS, Shin JW, Kang YG, Kim HK, Yoon TR, Shin J-W (2012) Scaffolds for bone tissue engineering fabricated from two different materials by the rapid prototyping technique: PCL *versus* PLGA. *J Mater Sci Mater Med* **23**: 2671-2678.
- Pedersen TO, Blois AL, Xing Z, Xue Y, Sun Y, Finne-Wistrand A, Akslen LA, Lorens JB, Leknes KN, Fristad I, Mustafa K (2013) Endothelial microvascular networks affect gene-expression profiles and osteogenic potential of tissue-engineered constructs. *Stem Cell Res Ther* **4**: 52. DOI: 10.1186/scrt202.
- Phelps EA, Garcia AJ (2009) Update on therapeutic vascularization strategies. *Regen Med* **4**: 65-80.
- Polini A, Pisignano D, Parodi M, Quarto R, Scaglione S (2011) Osteoinduction of human mesenchymal stem cells by bioactive composite scaffolds without supplemental osteogenic growth factors. *PLoS One* **6**: e26211. DOI: 10.1371/journal.pone.0026211.
- Quarto R, Mastrogiacomo M, Cancedda R, Kutepov SM, Mukhachev V, Lavroukov A, Kon E, Marcacci M (2001) Repair of large bone defects with the use of autologous bone marrow stromal cells. *N Engl J Med* **344**: 385-386.
- Rabie AB (1997) Vascular endothelial growth pattern during demineralized bone matrix induced osteogenesis. *Connect Tissue Res* **36**: 337-345.
- Rai B, Lin JL, Lim ZXH, Guldberg RE, Huttmacher DW, Cool SM (2010) Differences between *in vitro* viability and differentiation and *in vivo* bone-forming efficacy of human mesenchymal stem cells cultured on PCL-TCP scaffolds. *Biomaterials* **31**: 7960-7970.
- Rao RR, Peterson AW, Ceccarelli J, Putnam AJ, Stegemann JP (2012) Matrix composition regulates three-dimensional network formation by endothelial cells and mesenchymal stem cells in collagen/fibrin materials. *Angiogenesis* **15**: 253-264.
- Reddi AH (1998) Role of morphogenetic proteins in skeletal tissue engineering and regeneration. *Nat Biotechnol* **16**: 247-252.
- Reddi AH (2007) Morphogenesis and tissue engineering. In: *Principles of Tissue Engineering* (Lanza R, Langer R, Vacanti JP, eds), Elsevier Academic Press, London. pp: 117-118.
- Reichert JC, Wullschleger ME, Cipitria A, Lienau J, Cheng TK, Schutz MA, Duda GN, Noth U, Eulert J, Huttmacher DW (2011) Custom-made composite scaffolds for segmental defect repair in long bones. *Int Orthop* **35**: 1229-1236.
- Roy TD, Simon JL, Ricci JL, Rekow ED, Thompson VP, Parsons JR (2003) Performance of degradable composite bone repair products made *via* three-dimensional fabrication techniques. *J Biomed Mater Res A* **66**: 283-291.
- Samavedi S, Whittington AR, Goldstein AS (2013) Calcium phosphate ceramics in bone tissue

engineering: a review of properties and their influence on cell behavior. *Acta Biomater* **9**: 8037-8045.

Scherberich A, Galli R, Jaquier C, Farhadi J, Martin I (2007) Three-dimensional perfusion culture of human adipose tissue-derived endothelial and osteoblastic progenitors generates osteogenic constructs with intrinsic vascularization capacity. *Stem Cells* **25**: 1823-1829.

Schipani E, Maes C, Carmeliet G, Semenza GL (2009) Regulation of osteogenesis-angiogenesis coupling by HIFs and VEGF. *J Bone Miner Res* **24**: 1347-1353.

Seyednejad H, Gawlitta D, Kuiper RV, de Bruin A, van Nostrum CF, Vermonden T, Dhert WJ, Hennink WE (2012) *In vivo* biocompatibility and biodegradation of 3D-printed porous scaffolds based on a hydroxyl-functionalized poly(epsilon-caprolactone). *Biomaterials* **33**: 4309-4318.

Shayesteh YS, Khojasteh A, Soleimani M, Alikhasi M, Khoshzaban A, Ahmadbeigi N (2008) Sinus augmentation using human mesenchymal stem cells loaded into a  $\beta$ -tricalcium phosphate/hydroxyapatite scaffold. *Oral Surg Oral Med Oral Pathol Oral Radiol Endod* **106**: 203-209.

Shim J-H, Yoon M-C, Jeong C-M, Jang J, Jeong S-I, Cho D-W, Huh J-B (2014) Efficacy of rhBMP-2 loaded PCL/PLGA/ $\beta$ -TCP guided bone regeneration membrane fabricated by 3D printing technology for reconstruction of calvaria defects in rabbit. *Biomed Mater* **9**: 065006. DOI: 10.1088/1748-6041/9/6/065006.

Shor L, Gucer S, Chang R, Gordon J, Kang Q, Hartsock L, An Y, Sun W (2009) Precision extruding deposition (PED) fabrication of polycaprolactone (PCL) scaffolds for bone tissue engineering. *Biofabrication* **1**: 015003. DOI: 10.1088/1758-5082/1/1/015003.

Sultana N, Wang M (2008) Fabrication of HA/PHBV composite scaffolds through the emulsion freezing/freeze-drying process and characterisation of the scaffolds. *J Mater Sci Mater Med* **19**: 2555-2561.

Temple JP, Hutton DL, Hung BP, Huri PY, Cook CA, Kondragunta R, Jia X, Grayson WL (2014) Engineering anatomically shaped vascularized bone grafts with hASCs and 3D-printed PCL scaffolds. *J Biomed Mater Res A* **102**: 4317-4325.

Tyanova S, Temu T, Cox J (2016a) The MaxQuant computational platform for mass spectrometry-based shotgun proteomics. *Nat Protoc* **11**: 2301-2319.

Tyanova S, Temu T, Sinitcyn P, Carlson A, Hein MY, Geiger T, Mann M, Cox J (2016b) The Perseus computational platform for comprehensive analysis of (prote)omics data. *Nature Methods* **13**: 731-740.

Von Euw S, Wang Y, Laurent G, Drouet C, Babonneau F, Nassif N, Azaïs T (2019) Bone mineral: new insights into its chemical composition. *Sci Rep* **9**: 8456. DOI: 10.1038/s41598-019-44620-6.

Wang Y, Wan C, Deng L, Liu X, Cao X, Gilbert SR, Bouxsein ML, Faugere MC, Guldborg RE, Gerstenfeld LC, Haase VH, Johnson RS, Schipani E, Clemens TL (2007) The hypoxia-inducible factor alpha pathway

couples angiogenesis to osteogenesis during skeletal development. *J Clin Invest* **117**: 1616-1626.

Yang WC, Guo DY, Harris MA, Cui Y, Gluhak-Heinrich J, Wu JJ, Chen XD, Skinner C, Nyman JS, Edwards JR, Mundy GR, Lichtler A, Kream BE, Rowe DW, Kalajzic I, David V, Quarles DL, Villareal D, Scott G, Ray M, Liu S, Martin JF, Mishina Y, Harris SE (2013) Bmp2 in osteoblasts of periosteum and trabecular bone links bone formation to vascularization and mesenchymal stem cells. *J Cell Sci* **126**: 4085-4098.

Yeo A, Rai B, Sju E, Cheong JJ, Teoh SH (2008) The degradation profile of novel, bioresorbable PCL-TCP scaffolds: an *in vitro* and *in vivo* study. *J Biomed Mater Res A* **84**: 208-218.

Yeo A, Wong WJ, Teoh SH (2010) Surface modification of PCL-TCP scaffolds in rabbit calvaria defects: Evaluation of scaffold degradation profile, biomechanical properties and bone healing patterns. *J Biomed Mater Res A* **93**: 1358-1367.

Yilgor P, Sousa RA, Reis RL, Hasirci N, Hasirci V (2008) 3D plotted PCL scaffolds for stem cell based bone tissue engineering. *Macromol Symp* **269**: 92-99.

You MH, Kwak MK, Kim DH, Kim K, Levchenko A, Kim DY, Suh KY (2010) Synergistically enhanced osteogenic differentiation of human mesenchymal stem cells by culture on nanostructured surfaces with induction media. *Biomacromolecules* **11**: 1856-1862.

Zamiri B, Shahidi S, Eslaminejad MB, Khoshzaban A, Gholami M, Bahramnejad E, Moghadasali R, Mardpour S, Aghdami N (2013) Reconstruction of human mandibular continuity defects with allogenic scaffold and autologous marrow mesenchymal stem cells. *J Craniofac Surg* **24**: 1292-1297.

Zhao L, Liu L, Wu Z, Zhang Y, Chu PK (2012) Effects of micropitted/nanotubular titania topographies on bone mesenchymal stem cell osteogenic differentiation. *Biomaterials* **33**: 2629-2641.

Zhou T, Li C, Zhao W, Wang X, Wang F, Sha J (2016) MaxReport: an enhanced proteomic result reporting tool for MaxQuant. *PLoS One* **11**: e0152067. DOI: 10.1371/journal.pone.0152067.

## Discussion with Reviewers

**Andrea Vernengo:** Please justify the conclusion that the scaffolds enabled osteogenic differentiation of MSCs, with the cell studies that appeared to be conducted with one donor and no gene expression analysis performed.

**Authors:** As tissue engineers, our goal was to engineer functional bone tissue, hence the decision to use *in vivo* assays of implant vascularisation and bone formation as main assessment of osteogenic differentiation. For such *in vivo* assays,  $\mu$ CT and histology still provided the clearest indication of new bone deposition. Cell studies were only conducted with MSCs from the same donor. Understanding biological variability in response to these classes of biomaterial is worthy of further investigation.

**Matteo D'Este:** Do you think that the thermal treatment was degrading part of the bone matrix? Would such an approach be applicable to other polymers with a higher melting point or to hydrogel printing?

**Authors:** As we were 3D-printing with PCL, the temperatures required to print the thermopolymer was rather low (approximately 69 °C). Printing at this temperature did not seem to degrade the bone matrix, which remained osteoinductive. However, using it with thermopolymers with higher melting temperatures might prove difficult as the bone ECM

may lose some of its osteoinductive properties after being subjected to higher temperatures. Current ongoing studies have begun investigating adding the decellularised bone ECM into PLGA, which needs to be printed at a much higher melting point, and will investigate if the bone ECM still has its osteoinductive properties both *in vitro* and *in vivo*.

**Editor's note:** The Scientific Editor responsible for this paper was Mauro Alini.